MNRAS 000, 1–19 (2018) Preprint 22 January 2020 Compiled using MNRAS LATEX style file v3.0

Cosmological constraints from galaxy-lensing cross correlations using BOSS galaxies with SDSS and CMB lensing

Sukhdeep Singh[1,2⋆], Rachel Mandelbaum[2], Uroš Seljak[1], Sergio Rodríguez-Torres[3], Anže Slosar[4]

[1] *Berkeley Center for Cosmological Physics, University of California, Berkeley, CA 94720, USA*
[2] *McWilliams Center for Cosmology, Department of Physics, Carnegie Mellon University, Pittsburgh, PA 15213, USA*
[3] *Departamento de Física Teórica M8, Universidad Autónoma de Madrid (UAM), Cantoblanco, E-28049, Madrid, Spain*
[4] *Physics Department, Brookhaven National Laboratory, Upton, NY 11973, USA*

Accepted XXX. Received YYY; in original form ZZZ

ABSTRACT

We present cosmological parameter constraints based on a joint modeling of galaxy-lensing cross correlations and galaxy clustering measurements in the SDSS, marginalizing over small-scale modeling uncertainties using mock galaxy catalogs, without explicit modeling of galaxy bias. We show that our modeling method is robust to the impact of different choices for how galaxies occupy dark matter halos and to the impact of baryonic physics (at the $\sim 2\%$ level in cosmological parameters) and test for the impact of covariance on the likelihood analysis and of the survey window function on the theory computations. Applying our results to the measurements using galaxy samples from BOSS and lensing measurements using shear from SDSS galaxies and CMB lensing from Planck, with conservative scale cuts, we obtain $S_8 \equiv \left(\frac{\sigma_8}{0.8228}\right)^{0.8}\left(\frac{\Omega_m}{0.307}\right)^{0.6} = 0.85 \pm 0.05$ (stat.) using LOWZ $\times$ SDSS galaxy lensing, and $S_8 = 0.91 \pm 0.1$ (stat.) using combination of LOWZ and CMASS $\times$ Planck CMB lensing. We estimate the systematic uncertainty in the galaxy-galaxy lensing measurements to be $\sim 6\%$ (dominated by photometric redshift uncertainties) and in the galaxy-CMB lensing measurements to be $\sim 3\%$, from small scale modeling uncertainties including baryonic physics.

Key words: galaxies: evolution — cosmology: observations — large-scale structure of Universe — gravitational lensing: weak

1 INTRODUCTION

The ΛCDM cosmological model has been successful in explaining a wide array of cosmological observables. However, the model includes as yet poorly understood cold dark matter (CDM) and the cosmological constant, Λ (or dark energy in general). Both of these components affect the expansion history and the growth of structure in the Universe, which provides a promising avenue to probe them.

Gravitational lensing, the perturbations to the path of photons by the gravitational effects of matter, has emerged as an important probe of the geometry and the growth of structure in the universe (Bartelmann & Schneider 2001; Weinberg et al. 2013; Kilbinger 2015; Mandelbaum 2017). In the weak regime, lensing effects of the (foreground) matter introduce small and coherent perturbations in the light profiles of background objects. By measuring the correlations between shapes or sizes of background galaxies (or CMB perturbations when using CMB lensing), we can infer the structure in the distribution of foreground matter. By selecting sources at different distances or redshifts, weak lensing also enables the study of growth and evolution of structure in the universe. Several studies have used the correlations in the shapes of galaxies (cosmic shear, or shear-shear correlations) to probe the growth history of the Universe (e.g., Semboloni et al. 2006; Massey et al. 2007; Kitching et al. 2014; Hildebrandt et al. 2016; van Uitert et al. 2017; DES Collaboration et al. 2017) and more recently there have been similar studies using the lensing of CMB (e.g., Das et al. 2011; Planck Collaboration et al. 2014b, 2015; Omori et al. 2017; Sherwin et al. 2017).

The cross correlations between the galaxies and the

⋆ sukhdeep1@berkeley.edu

lensing maps provide another avenue to probe the distribution of matter around galaxies. The galaxy-galaxy lensing cross correlation have been used by several studies to probe the connection between the galaxies and their host halos (e.g., Hoekstra et al. 2004; Mandelbaum et al. 2006; Heymans et al. 2006; Tinker et al. 2012; Leauthaud et al. 2012; van Uitert et al. 2012; Gillis et al. 2013; Velander et al. 2014; Sifón et al. 2015; Hudson et al. 2015; van Uitert et al. 2016; Dvornik et al. 2018). Combined with galaxy clustering, these measurements also provide a measure of the matter correlations (matter power spectrum), independent of the galaxy bias. These measurements have been widely used to measure the cosmological parameters, especially the amplitude of the matter power spectrum quantified by σ_8 at various redshifts (Seljak et al. 2005; Baldauf et al. 2010; Mandelbaum et al. 2013; More et al. 2015; Kwan et al. 2016; Buddendiek et al. 2016). Similar studies have also been performed using CMB lensing (Hand et al. 2015; Giannantonio et al. 2016; Kirk et al. 2016; Singh et al. 2017a). Furthermore, combined with other probes of large scale structure, such as redshift space distortions, these measurements can also be used to test theories of gravity (e.g., Zhang et al. 2007; Reyes et al. 2010; Blake et al. 2016; Alam et al. 2017; Pullen et al. 2016; Singh et al. 2018).

When extracting cosmological information from galaxy clustering and galaxy-galaxy lensing, an important limiting factor is the difficulty in modeling the correlations at smaller spatial scales. Models for correlations in the matter density field that are based on perturbation theory tend to fail at small scales (see Bernardeau et al. 2002, for review) and it is also difficult to predict the non-linear galaxy bias and the stochastic cross correlations between the galaxies and matter. A conservative solution is to only use the measurement on large scales where the model is reliable, though this can involve a considerable loss of information from small scales, where having more modes results in better signal-to-noise measurements. To model the small scales, one must resort to modeling based on N-body simulations using tools such as Halo Occupation and Distribution (HOD) models, which provide a framework to populate halos with galaxies (see Cooray & Hu 2001, for review). HOD-based modeling has been used by Seljak et al. (2005); Cacciato et al. (2009, 2013); More et al. (2015) to derive cosmological parameter constraints (see also Wibking et al. 2017).

While HOD modeling provides an effective and potentially flexible way of modeling the observables, it requires assumptions about the relationships between the galaxies and their host halos and then marginalizes over model parameters describing those relationships. These assumptions in turn can affect the cosmological inferences. While a more flexible HOD can in principle provide sufficient model freedom to reduce biases substantially, having a very flexible HOD can result in loss of information. In contrast, having too inflexible model can result in overly optimistic and potentially biased inferences.

Another approach to extracting information from smaller scales is to model the matter power spectrum to smaller scales using emulators trained on N-body simulations but also remove the information from small scales that are strongly affected by the stochastic relation between galaxies and matter. One such approach, suggested by Baldauf et al. (2010), involves removing the small scale information from the lensing observables and then modeling the remaining linear and quasi-linear scales using a simulation-based emulator or higher order perturbation theory. This approach was successfully applied by Mandelbaum et al. (2013); Singh et al. (2017a) to derive cosmological parameters and by several papers to test gravity using the E_G parameter (Reyes et al. 2010; Blake et al. 2016; Alam et al. 2017; Singh et al. 2018).

In this work, we develop the methodology to derive the cosmological parameters from the combination of galaxy clustering and galaxy-lensing cross correlations following the approach of Baldauf et al. (2010), but without having to explicitly model the galaxy bias. We model the galaxy-matter cross correlation coefficient (which can be thought of as the difference in non-linear bias between galaxy-galaxy and galaxy-matter correlations) using simulations. We will also extend the results using the estimator proposed by Baldauf et al. (2010) down to smaller scales than has been done before.

We begin by describing the lensing and clustering formalism as well as the estimators used to measure the signals in section 2 followed by the description of modeling schemes in section 3. We describe the datasets and mock datasets used for measurements in section 4. Results from fitting the measurements from both data and mock galaxy catalogs are presented in section 5 and we conclude in section 6.

Throughout we use $\Omega_m = 0.307, \sigma_8 = 0.8228, h = 0.6777, n_s = 0.96$ (Planck Collaboration et al. 2014a) as our fiducial cosmology, and express comoving distances in units of h^{-1}Mpc.

2 FORMALISM AND METHODOLOGY

In this section we review the basic formalism of galaxy clustering and galaxy-lensing cross correlation measurements as well as the estimator used for the measurements.

2.1 Weak Lensing

The gravitational lensing effects of the foreground matter distribution introduce small but coherent distortions in the light profiles of the background objects (see Bartelmann & Schneider 2001; Weinberg et al. 2013, for review). The gravitational lensing measurements are sensitive to the lensing potential defined as

$$\Phi_L = \int d\chi_l \frac{f_\kappa(\chi_s - \chi_l)}{f_\kappa(\chi_s) f_\kappa(\chi_l)} \Psi(f_\kappa(\chi_l)\vec{\theta}, \chi_l), \tag{1}$$

where the Weyl potential $\Psi = \psi + \phi$, and ϕ and ψ are the Newtonian and curvature potentials. χ_s and χ_l are line-of-sight comoving distances to source and lens redshifts and $f_k(\chi)$ are the transverse comoving distances. Within GR, $\phi = \psi$ and $\nabla^2\phi = 4\pi G\rho_m$. The Jacobian of relating image to source locations is

$$A_{ij} = \frac{\partial(\theta_o^i - \delta\theta_o^i)}{\partial\theta_o^j}, \tag{2}$$

$$A_{ij} = \delta_{ij} - \frac{\partial^2\Phi_l}{\partial\theta_o^i\partial\theta_o^j}, \tag{3}$$

$$A = \begin{bmatrix} 1-\kappa-\gamma_1 & -\gamma_2 \\ -\gamma_2 & 1-\kappa+\gamma_1 \end{bmatrix}$$

. The primary weak gravitational lensing observables are the convergence κ and the shear $\gamma = \gamma_1 + \mathrm{i}\gamma_2$, defined as

$$\kappa = -\frac{1}{2}\nabla_\perp^2\Phi_L \leftrightarrow \frac{1}{2}k_\perp^2\Phi_L, \tag{4}$$

$$\gamma_1 = \frac{1}{2}(\nabla_{1,1}^2 - \nabla_{2,2}^2)\Phi_L \leftrightarrow \frac{1}{2}(k_{\perp,1}^2 - k_{\perp,2}^2)\Phi_L, \tag{5}$$

$$\gamma_2 = \frac{1}{2}(\nabla_{1,2}^2)\Phi_L \leftrightarrow \frac{1}{2}(k_{\perp,1}k_{\perp,2})\Phi_L, \tag{6}$$

where derivatives are with respect to the projected (perpendicular to line of sight) coordinates and we have used $\leftrightarrow$ to denote equivalent Fourier space counterparts.

2.1.1 *Galaxy lensing cross correlations*

Galaxy lensing cross correlations measure the projected surface mass density, Σ, around the galaxies, which is related to convergence and shear as

$$\kappa(r_p) = \frac{\Sigma(r_p)}{\Sigma_c}, \tag{7}$$

$$\gamma_t(r_p) = \frac{\overline{\Sigma}(<r_p) - \Sigma(r_p)}{\Sigma_c}. \tag{8}$$

$\overline{\Sigma}(<r_p)$ is the mean surface mass density within the radius r_p with the critical density, Σ_c defined as

$$\Sigma_c = \frac{c^2}{4\pi G}\frac{f_k(\chi_s)}{(1+z_l)f_k(\chi_l)f_k(\chi_s-\chi_l)}. \tag{9}$$

Σ is related to the projected galaxy-matter cross correlations as

$$\Sigma(r_p) = \bar{\rho}_m \int \mathrm{d}\Pi\, \xi_{gm}(r_p,\Pi) = \bar{\rho}_m w_{gm}(r_p). \tag{10}$$

The matter-galaxy correlation function, ξ_{gm}, can further be related to the matter power spectrum as

$$\xi_{gm}(r_p,\Pi) = b_g(r_p)r_{cc}(r_p)\int \mathrm{d}z W_L(z)\int \frac{\mathrm{d}^2k_\perp dk_z}{(2\pi)^3} \times P_{\delta\delta}(\vec{k},z)e^{\mathrm{i}(\vec{r}_p.\vec{k}_\perp+\Pi k_z)}, \tag{11}$$

where $b_g(r_p)$ is the galaxy bias and $r_{cc}(r_p)$ is the galaxy-matter cross correlation coefficient and are defined as

$$b_g(r_p) = \sqrt{\frac{\xi_{gg}(r_p)}{\xi_{mm}(r_p)}}, \tag{12}$$

$$r_{cc}(r_p) = \frac{\xi_{gm}(r_p)}{\sqrt{\xi_{gg}(r_p)\xi_{mm}(r_p)}}. \tag{13}$$

The weight function $W_L(z)$ denotes the effective weight/contribution from lens galaxies at each redshift to the measured signal and is given as

$$W_L(z_l) = p(z_l)\int_{z_l}^{\infty} dz_s p(z_s)\Sigma_c(z_l,z_s)w_{ls} \tag{14}$$

where $p(z_l)$ and $p(z_s)$ are the redshift distributions of lens and source galaxies (in the case of galaxy lensing) respectively, Σ_c is the critical density (lensing kernel) for the lens-source pair and w_{ls} is the lens-source pair weights used in the estimators when measuring the signal (see Section 2.3).

2.2 Galaxy Clustering

The two-point correlation function of galaxies is given by

$$\xi_{gg}(r_p,\Pi) = b_g^2(r_p)\int \mathrm{d}z W(z)\int \frac{\mathrm{d}^2k_\perp \mathrm{d}k_z}{(2\pi)^3} \times P_{\delta\delta}(\vec{k},z)(1+\beta\mu_k^2)^2 e^{\mathrm{i}(\vec{r}_p.\vec{k}_\perp+\Pi k_z)}. \tag{15}$$

The Kaiser factor, $(1+\beta\mu_k^2)$ accounts for the redshift space distortions (Kaiser 1987), where $\beta = f(z)/b_g$, $f(z)$ is the linear growth rate factor at redshift z and $\mu_k = k_z/k$. The weight function[1] $W(z)$ denotes the effective weight/contribution of galaxies at each redshift to the measured signal and is given by Mandelbaum et al. (2011) as

$$W(z) = \frac{p(z)^2}{\chi^2(z)\mathrm{d}\chi/\mathrm{d}z}\left[\int \frac{p(z)^2}{\chi^2(z)\mathrm{d}\chi/\mathrm{d}z}\mathrm{d}z\right]^{-1}. \tag{16}$$

$p(z)$ is the redshift probability distribution for the galaxy sample.

Finally we integrate ξ_{gg} over the line-of-sight separation to get the projected correlation function

$$w_{gg}(r_p) = \int_{-\Pi_{\max}}^{\Pi_{\max}} \mathrm{d}\Pi\, \xi_{gg}(r_p,\Pi). \tag{17}$$

The choice of $\Pi_{\max}$ depends on the impact of redshift space distortions (RSD), which leads to a need for large $\Pi_{\max}$ especially when going to large r_p, and the increase of noise in the final measurement, which increases with $\Pi_{\max}$. We choose $\Pi_{\max} = 100h^{-1}$Mpc and then apply the corrections for RSD to the measured projected correlation function using the Kaiser factor. As was shown in Singh et al. (2018) this correction is much smaller than the statistical errors on the scales we use and has a negligible effect on our final results.

2.3 Estimators

In this section we present the estimators used for measuring various signals. For all of the measurements, we use 100 approximately equal-area (~ 8 degrees on a side) jackknife regions to obtain the jackknife mean and covariance (see Singh et al. 2017a,b, for more details).

2.3.1 *Galaxy-Galaxy Lensing*

For galaxy-galaxy lensing, we measure the excess surface density $\Delta\Sigma$ as

$$\widehat{\Delta\Sigma}(r_p) = B_L(1+m_\gamma)\left[\frac{\sum_{ls} w_{ls}e_t^{(ls)}\Sigma_{\rm crit}^{(ls)}}{2\mathcal{R}\sum_{rs}w_{rs}} - \frac{\sum_{rs} w_{rs}e_t^{(rs)}\Sigma_{\rm crit}^{(rs)}}{2\mathcal{R}\sum_{rs}w_{rs}}\right]. \tag{18}$$

The summation is over all lens-source (ls) and random-source (rs) pairs. e_t is the tangential ellipticity measured in the lens-source frame, m_γ is the multiplicative bias in

[1] Note that here we assume that the correlations for a given galaxy only contain contributions from modes at the same redshift as the galaxy, which then allows us to separate the integrals over redshift and k_z.

our shear estimates and $\mathcal{R}$ is the responsivity factor to convert the ensemble average of ellipticities to shear. B_L is the calibration factor to account for bias due to photometric redshift of source galaxies. The weight w_{rs} in the denominator of Eq. (18) accounts for the source galaxies associated with the lens, which do not contribute any shear but are counted in the total weights. The correction factor for this effect w_{ls}/w_{rs} is usually called the boost factor (Sheldon et al. 2004; Mandelbaum et al. 2005). Finally, we also subtract the shear signal measured around the random points for two reasons: to remove systematics that can give some spurious shear signal at large scales, and for the optimal covariance of the final measurements (Singh et al. 2017b). The weight w_{ls} for each lens-source pair is defined as

$$w_{ls} = \frac{w_l \Sigma_c^{-2}}{\sigma_\gamma^2 + \sigma_{SN}^2}. \tag{19}$$

The Σ_c^{-2} in the weight is required for the optimal estimator in the shape noise-dominated regime (Sheldon et al. 2004), w_l is the weight assigned to lens galaxies (systematic weights for BOSS galaxies, see section 4.1.1), σ_γ is the measurement noise for the galaxy shape and σ_{SN} is the shape noise.

2.3.2 *Galaxy-CMB lensing*

From CMB lensing maps, we get estimates of the convergence, from which we measure the projected surface mass density around galaxies as (Singh et al. 2017a)

$$\widehat{\Sigma}(r_p) = \frac{\sum_{lp} w_{lp}\kappa_p \Sigma_{c,*}}{\sum_{lp} w_{lp}} - \frac{\sum_{Rp} w_{Rp}\kappa_p \Sigma_{c,*}}{\sum_{Rp} w_{Rp}}, \tag{20}$$

where the summation is over all the lens-pixel (pixels of CMB convergence map) pairs at separations $r_p \in [r_{p,min}, r_{p,max}]$ at the lens redshift and the signal around random points is subtracted to achieve a more optimal measurement (Singh et al. 2017b). $\Sigma_{c,*}$ is $\Sigma_{\rm crit}$ with CMB as the source.

Similar to the galaxy-galaxy lensing case, the weight for each lens-pixel pair is given by

$$w_{lp} = w_l \Sigma_{c,*}^{-2}. \tag{21}$$

2.3.3 *Galaxy Clustering*

We use the Landy-Szalay (Landy & Szalay 1993) estimator to compute the galaxy two-point correlation function:

$$\xi_{gg}(r_p, \Pi) = \frac{DD - 2DR + RR}{RR}, \tag{22}$$

where D is the weighted galaxy sample, with weights defined in Section 4.1.1 and R is for the random point sample (corresponding to the weighted galaxy catalog). The projected correlation function is obtained by integrating over the bins in line-of-sight separation, Π

$$w_{gg}(r_p) = \sum_{-\Pi_{\rm max}}^{\Pi_{\rm max}} \Delta\Pi\, \xi_{gg}(r_p, \Pi). \tag{23}$$

We use $\Pi_{\rm max} = 100h^{-1}$Mpc, with 20 bins of size $\Delta\Pi = 10h^{-1}$Mpc. $\Pi_{\rm max} = 100h^{-1}$Mpc is large enough so that the effects of redshift space distortions are small and avoids including very large line of sight scales which contribute little to the signal but increase the noise (see more discussion in Singh et al. 2018)

2.4 Removing small scale information

We use the estimator suggested by Baldauf et al. (2010) to remove the difficult-to-model small-scale information from $\Delta\Sigma$

$$\Upsilon_{gm}(r_p, r_0) = \Delta\Sigma(r_p) - \left(\frac{r_0}{r_p}\right)^2 \Delta\Sigma(r_0). \tag{24}$$

$\Sigma(r_p)$ and w_{gg} ($\Sigma_{gg} = \bar{\rho}_m w_{gg}$) can also be converted to Υ using the relations between Σ and $\Delta\Sigma$ and corresponding theoretical calculations can be done. In addition to removing the small scale information, Baldauf et al. (2010) also showed that Υ reduces the impact of sample variance and the redshift space distortions in the projected correlation functions. We will use Υ as well as $\Delta\Sigma$ with a model inspired from Υ in our analysis. To compute Υ, we also need to choose the scale r_0 below which all the information is removed. We will try few different values of r_0, with the aim of choosing to smallest possible r_0 values for which we can obtain unbiased results on the cosmological parameters in the mock galaxy catalogs.

3 MODELLING

In this section we describe three different methods to model the observables, $\Upsilon_{\rm gm}$ or $\Delta\Sigma_{gm}$, while removing the information from small scales. In short, we will model the galaxy-lensing cross correlations in terms of galaxy and matter clustering. where matter clustering is predicted using analytical model and galaxy clustering is directly taken from the measurements. We will use the non-linear matter power spectrum computed using halofit (Takahashi et al. 2012) using CLASS (Lesgourgues 2011). In the current approach, we will be ignoring the covariance of galaxy clustering since the galaxy correlation functions are measured to much better precision than the galaxy-lensing cross correlations. We will later test these models on mock galaxy catalogs, which will also allow us to choose the values of the cutoff scale r_0.

3.1 Modelling Υ_{gm}

We write the model for galaxy-matter correlations Υ_{gm} in terms of the clustering of galaxies, Υ_{gg} and matter, Υ_{mm}, as:

$$\Upsilon_{gm} = \bar{\rho}_m r_{cc}^{(\Upsilon)} \sqrt{\Upsilon_{mm}\Upsilon_{gg}}, \tag{25}$$

where $r_{cc}^{(\Upsilon)}$ is the cross correlation coefficient between the galaxies and matter when using the Υ estimator. We also assume Υ_{gg} and Υ_{mm} are in units of length (no factors of density) and hence multiply with $\bar{\rho}_m$ to get the units of projected surface mass density.

We model r_{cc} as

$$r_{cc}(r_p) = 1 + \frac{a}{r_p^2 + b}, \tag{26}$$

where a, b are free parameters to be fit during the likelihood analysis to obtain cosmological parameters. We also estimate the range of values r_{cc} can take as a function of scale in mock galaxy catalogs and put (uniform) priors to constrain r_{cc} to stay within that range (note that the prior is on r_{cc} as a function of scale and not on a, b, see Fig. 6). We note that the choice of functional form in Eq. (26) is

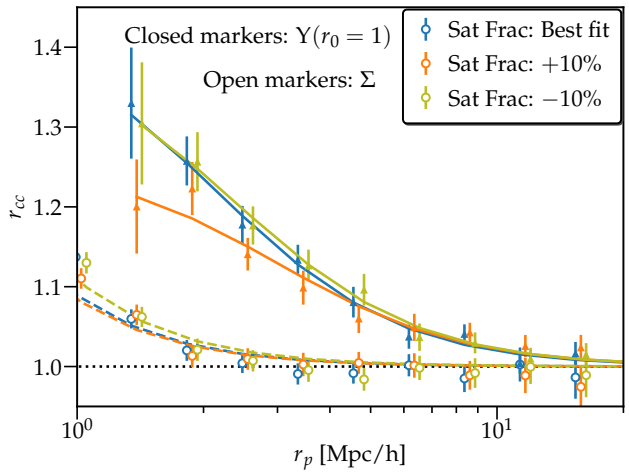

Figure 1. Galaxy-matter cross-correlation coefficient r_{cc} estimates from mock galaxy catalogs with different satellite fractions (see Section 4.2) and parametric model fits from eq. (26). Closed triangles show the r_{cc} estimates using the Υ estimator and open circles are using the Σ. This plot illustrates that the functional form adopted is sufficiently flexible to describe the behavior found in simulations, but we stress that the detailed form of r_{cc} is not important, as we find small shifts ($\lesssim 0.3\sigma$) in our results for cosmological parameters even when assuming $r_{cc} = 1$ on all scales used.

arbitrary, chosen to fit the shape of r_{cc} observed in simulations. In Fig. 1 we show that this particular functional form is sufficiently flexible to fit r_{cc} estimates from the variety of mock galaxy catalogs described in Section 4.2. We have also tested our results with some other functional forms (not shown in this paper) with similar shapes, and our results are not affected by this particular choice.

3.2 Modelling $\Delta\Sigma$

3.2.1 Model using Υ_{gm} ($\Delta\Sigma_{gm} \leftarrow \Upsilon_{gm}$)

Using the prediction of $\Upsilon_{\rm gm}$ from Eq. (25), we can predict $\Delta\Sigma_{gm}$ as

$$\Delta\Sigma_{gm}(r_p) = \Upsilon_{gm}(r_p) + \frac{r_0^2}{r_p^2}\Delta\Sigma_0, \tag{27}$$

where $\Delta\Sigma_0$ is an additional free parameter to be marginalized over.

3.2.2 Model using Σ ($\Delta\Sigma_{gm} \leftarrow \Sigma_{gm}$)

One of the motivations to use Υ parameter is to remove the information from scales where the r_{cc} value deviates significantly from 1. To include some scales where r_{cc} deviates from 1, one can also predict $\Delta\Sigma$ directly from Σ, where r_{cc} values are more localized in r_p (i.e. deviate from 1 at smaller r_p) compared to $\Delta\Sigma$ and Υ. In this case we begin by predicting Σ_{gm},

$$\Sigma_{gm} = r_{cc}^{(\Sigma)}\sqrt{\Sigma_{mm}\Sigma_{gg}}, \tag{28}$$

where we use same model as in Eq. (26) to predict $r_{cc}^{(\Sigma)}$ and also put priors on $r_{cc}^{(\Sigma)}$ based on the range of values observed in mock galaxy catalogs.

Σ_{gm} can then be converted to $\Delta\Sigma$ as

$$\Delta\Sigma_{gm}(r_p) = \frac{1}{r_p^2}\int_{r_0}^{r_p} {\rm d}r_p' r_p' \Sigma_{gm} + \frac{1}{r_p^2}\Sigma_0 - \Sigma_{gm}(r_p). \tag{29}$$

Notice that we have restricted the integrals over predicted Σ_{gm} on scales $> r_0$ and also introduced the parameter Σ_0, which is the integrated Σ_{gm} over scales $< r_0$.

$$\Sigma_0 = \int_0^{r_0} dr_p' r_p' \Sigma_{gm} = r_0^2(\Delta\Sigma_{gm}(r_0) + \Sigma_{gm}(r_0)). \tag{30}$$

4 DATA

4.1 SDSS

The SDSS survey (Gunn et al. 1998; York et al. 2000; Hogg et al. 2001; Ivezić et al. 2004; Fukugita et al. 1996; Smith et al. 2002; Eisenstein et al. 2001; Gunn et al. 2006; Richards et al. 2002; Strauss et al. 2002) was an imaging and spectroscopic survey, which has imaged approximately quarter of the sky, and has produced imaging catalogs (Lupton et al. 2001; Pier et al. 2003; Tucker et al. 2006; Abazajian et al. 2009; Aihara et al. 2011; Padmanabhan et al. 2008) which have also been used for target selection for the spectroscopic follow up in the BOSS survey as well as generation of the shear catalogs described in this section.

4.1.1 SDSS-III BOSS

As tracers for the galaxy density field, we use SDSS-III BOSS (Blanton et al. 2003; Bolton et al. 2012; Ahn et al. 2012; Dawson et al. 2013; Smee et al. 2013) data release 12 (DR12; Alam et al. 2015) LOWZ galaxies, in the redshift range $0.16 < z < 0.36$ and CMASS galaxies in the redshift range $0.43 < z < 0.7$. We apply the systematic weights for the galaxies when computing both galaxy clustering and the galaxy lensing cross correlations (w_l as defined in section 2.3), where the weights are given by (Ross et al. 2012)

$$w_l = w_{\rm sys}(w_{no-z} + w_{cp} - 1), \tag{31}$$

where $w_{\rm sys}$ weights correct for the variations in the selection function on the sky (important for CMASS) and w_{no-z}, w_{cp} correct for missing redshifts due to failure to obtain redshift (no-z) or fiber collisions for close pairs, *cp*. Impact of these weights on galaxy-lensing cross correlations was studied in Singh et al. (2017a).

4.1.2 Re-Gaussianization Shapes

The shape sample used to estimate the shear is described in more detail in Reyes et al. (2012). Briefly, these shapes are measured using the re-Gaussianization technique developed by Hirata & Seljak (2003). The algorithm is a modified version of ones that use "adaptive moments" (equivalent to fitting the light intensity profile to an elliptical Gaussian), determining shapes of the PSF-convolved galaxy image based on adaptive moments and then correcting the resulting shapes based on adaptive moments of the PSF. The re-Gaussianization method involves additional steps to correct for non-Gaussianity of both the PSF and the galaxy

surface brightness profiles (Hirata & Seljak 2003). The components of the distortion are defined as

$$(e_+, e_\times) = \frac{1-(b/a)^2}{1+(b/a)^2}(\cos 2\phi, \sin 2\phi), \quad (32)$$

where b/a is the minor-to-major axis ratio and ϕ is the position angle of the major axis on the sky with respect to the RA-Dec coordinate system. The ensemble average of the distortion is related to the shear as

$$\gamma_+, \gamma_\times = \frac{\langle e_+, e_\times \rangle}{2\mathcal{R}}; \quad (33)$$

$$\mathcal{R} = 1 - \frac{1}{2}\langle e_{+,i}^2 + e_{\times,i}^2 - 2\sigma_i^2 \rangle, \quad (34)$$

where σ_i is the per-component measurement uncertainty of the galaxy distortion, and $\mathcal{R} \approx 0.87$ is the shear responsivity representing the response of an ensemble of galaxies with some intrinsic distribution of distortion values to a small shear (Kaiser et al. 1995; Bernstein & Jarvis 2002).

4.2 Redshift-dependent mock galaxy catalogs

To get a prior on r_{cc} models as well as to test our models, we use the mock galaxy catalogs described here.

The clustering evolution and the abundance of galaxies as a function of redshift are modeled in light-cone catalogues drawn from the BigMultiDark simulation (BigMDPL; Klypin et al. 2016). This 2.5 h^{-1} Gpc simulation with 3840^3 particles adopts a ΛCDM model using the Planck 2013 cosmological parameters (Planck Collaboration et al. 2014a). In order to identify dark matter halos, the simulation implements the Robust Overdensity Calculation using K-Space Topologically Adaptive Refinement (ROCKSTAR) halo finder (Behroozi et al. 2013). The BigMDPL simulation has a volume large enough to construct a light-cone in the whole redshift range covered by the BOSS sample ($0.16 < z < 0.7$) with an area of $10,206$ deg^2. Additionally, this simulation was designed to resolve halos that host CMASS galaxies ($M_h > 2.5 \times 10^{12} M_\odot/h$, Shan et al. 2017), being 95% complete at $M_{vir} = 2 \times 10^{12} M_\odot/h$. It allows us to reproduce the observed clustering without including halos from the incomplete region of this simulation. The mean halo mass for the LOWZ like sample $\sim 3.1 \times 10^{13} M_\odot/h$ and for CMASS sample is $\sim 2.4 \times 10^{13} M_\odot/h$, which are larger than the masses estimated in Singh et al. (2017a) using weak lensing, $M_{\rm halo} \sim 10^{13} M_\odot/h$ for the LOWZ sample using SDSS galaxy lensing (note that the masses obtained using CMB lensing in Singh et al. 2017a are not reliable due to the resolution of the Planck CMB lensing map).

Galaxies are assigned to dark matter halos using a Sub Halo Abundance Matching (SHAM; Kravtsov et al. 2004; Conroy et al. 2006; Reddick et al. 2013) technique. This process is implemented by using the SUrvey GenerAtoR code (SUGAR; Rodríguez-Torres et al. 2016). The scatter between dark matter halos and galaxies is fixed to reproduce the projected correlation function of the BOSS data at different redshifts. Additionally, we fix the number density at each redshift in order to replicate the observed radial selection function. We perform the method using the maximum circular velocity over the whole history of the halo (V_{peak}) as the proxy for the mass of the dark matter halos hosting galaxies. In order to select halos hosting CMASS galaxies, we create a new variable $V_{new} = (1 + \mathcal{N}(\sigma_{\rm HAM}))V_{peak}$, where $\mathcal{N}$ is a random number from a Gaussian distribution with mean 0 and standard deviation $\sigma_{\rm HAM}$. Then, we rank-order halos based on V_{new} and select a number above a threshold in V_{new} tuned to achieve the desired number density. In this procedure we do not distinguish between host and subhalos, so the fraction of subhalos in the light-cone is given by the simulations. This methodology reproduces with a good agreement the small scales of both samples, with 11.4% and 12.3% of subhalos in the CMASS and LOWZ lightcones respectively.

We construct CMASS and LOWZ light-cones including all the available snapshots (40), which allows for a correct evolution of the dark matter along the line of sight. In order to reproduce the evolution of the observed clustering, we implement a SHAM model in six redshift bins using a different scatter value for each one. This is due to the dependency of the scatter with the circular velocity presented in the methodology used in the construction of our mock. However, our performance allows us to select the dark matter halos hosting LRGs using their abundance and clustering signal, without any stellar mass (or luminosity) information. (see Nuza et al. 2013).

Many studies have used SHAM models to study LRG galaxies for different stellar mass cuts (e.g. Reddick et al. 2013; Tinker et al. 2017), ensuring that the observed sample is complete for the given stellar mass cuts. In these cases, the clustering is described by the number density and the intrinsic scatter between galaxies and halos. Nevertheless, the BOSS sample is not complete for all stellar masses, so we have to take it into account for the construction of our mock. Different studies have included the incompleteness of the sample using stellar mass information (e.g. Saito et al. 2016; Rodríguez-Torres et al. 2016); however, we include this effect without using a proxy for galaxy mass, by increasing the value of scatter. This allows us approximately to mimic the incompleteness, including less massive halos in the final catalogue. Thus, the scatter used to reproduce the clustering in each redshift is combining the effect of the intrinsic relationship between galaxies and halos and the incompleteness of the sample. Most of the values of scatter are found to vary between 0.1 and 0.24, with an exception at high redshift ($0.57 < z < 0.7$) where the scatter is $0.55 \times V_{peak}$. Nevertheless, this is expected, since the abundance of galaxies is lower at this redshift (the mean stellar mass is higher than in other redshifts), while the clustering signal is relatively consistent with the clustering at other redshifts. The scatter values used and their dependence on redshift can be seen in Table 1.

Additionally, we produce light-cones with different satellite fractions. This is done by applying the same scatter for subhalos and host halos, such as in the standard HAM, but in this case, we include a new parameter to select a certain fraction of subhalos. The fraction of satellites of the standard HAM is varied by ±10% and ±15%, that means, an increase of 10% modifies the subhalo fraction of the LOWZ like sample from 12.3% to 13.5%. Note that there are additional selection effects such as mass and color dependent incompleteness that can potentially modify the galaxy clustering and galaxy-matter cross correlations on small scales (Leauthaud et al. 2017). In this work we are primarily interested in testing the variations on r_{cc} at scales $r_p > 1h^{-1}$Mpc

sample	z range	$\sigma_{\rm HAM}$	$\bar{n}$ ($10^{-4}{\rm Mpc}^{-3}h^3$)
LOWZ	0.16-0.24	0.26	4.10
	0.24-0.30	0.10	3.05
	0.30-0.36	0.14	3.29
CMASS	0.43-0.51	0.31	3.26
	0.51-0.57	0.24	3.66
	0.57-0.70	0.55	1.43

Table 1. Observed number density and scatter values used to select the halos hosting CMASS galaxies in six different redshift ranges.

at fixed clustering, where we expect that impact of these effects to be small on top of the variations introduced by varying satellite fractions.

5 RESULTS

In this section we first present the results of the analysis on mock galaxy catalogs, testing the impact of different estimators, and other modeling assumptions (see also the appendices) and then we present the results of analysis on the data, using both galaxy lensing and CMB lensing. Throughout this section we define $S_8 = \left(\frac{\sigma_8}{0.8228}\right)^{0.8}\left(\frac{\Omega_M}{0.307}\right)^{0.6}$, where the normalization factors for σ_8 and Ω_M are chosen based on the cosmology in the mock samples. We obtain the parameter likelihoods using MCMC with flat priors on $A_s \in [10^{-10}, 10^{-8}]$ and $\Omega_m \in [0.05, 0.75]$ and scale-dependent priors on r_{cc}. We fix other cosmological parameters and we do not impose any limits on $\Delta\Sigma_0$, as well as the parameters for the r_{cc} fitting function (eq. 26).

5.1 Analysis of mock galaxy catalogs

In this section we present the results from fitting the models presented in Section 3 to the measurements from mock galaxy catalogs described in Section 4.2

Fig. 2 shows the results of fitting measurements in mock catalogs using different models and using the jackknife covariance from the mock galaxy catalogs (no shape noise). We get consistent best fit values as well as consistent signal to noise ratio ($S/N \sim 70$) with different estimators and the results are consistent with the fiducial model.

Fig. 3 shows the comparison between mock galaxy catalogs and model predictions as well as residuals between the two. Model predictions are consistent with mock catalogs within the noise and we observe no trends in the residuals. These results suggest that our model works well down to $\sim 1h^{-1}$Mpc scale, though it not very surprising since we are using the priors on r_{cc} derived from the mock catalogs used themselves. In Appendix A we show results with a different set of mock catalogs, with different satellite fraction and r_{cc}, where we obtain consistent results using $r_0 = 2h^{-1}$Mpc and slightly biased results ($\sim 1\sigma$) using $r_0 = 1h^{-1}$Mpc. For most of the tests in this section, we will continue to use the more aggressive choice of $1h^{-1}$Mpc, though for the main results using the data we will show results with both $r_0 = 1h^{-1}$Mpc and $2h^{-1}$Mpc.

In Fig. 4, we show the derivatives of the different models with respect to different parameters. The sensitivity of the model to cosmological parameters increases as we go to smaller scales. However, small scales are also very sensitive to $\Delta\Sigma_0$ which suggests that some small-scale information is used in determining $\Delta\Sigma_0$. On the scales that we use, the model is relatively less sensitive to the r_{cc} parameters. In the following sections we explore the impact of some of the choices in the analysis in more detail. We further show some tests based on a different set of mock galaxy catalogs in Appendix A which highlight the impact of different choices of r_0 values. In Appendix B we show that the different covariances (jackknife and analytical) give consistent results. In Appendix C using a toy model we show that baryonic effects can introduce biases of up to 2% in S_8. Parameter values obtained using different modeling assumptions are shown in Table 2 and also on the figures showing different tests.

5.1.1 *Impact of $\Delta\Sigma_0$ or Σ_0*

In Fig. 5, we show the comparison of constraints for fixed $\Delta\Sigma_0$ versus marginalizing over $\Delta\Sigma_0$ when fitting $\Delta\Sigma$. Note that we do not impose any limits on $\Delta\Sigma_0$ in the likelihood analysis and when fixing $\Delta\Sigma_0$ we obtain the $\Delta\Sigma_0$ value at fixed cosmology and r_{cc} (r_{cc} is fixed to its value for the mock galaxy catalogs and we checked that the $\Delta\Sigma_0$ value obtained in this procedure is consistent with the measured value from mock catalogs). With fixed $\Delta\Sigma_0$, the S/N in S_8 for the two different models to fit $\Delta\Sigma$ is different by $\sim 30\%$. This is likely due to the projection effects onto S_8 plane, though the two models also have different sensitivity to the $\Delta\Sigma_0$ as shown in Fig. 4 which can contribute to these differences. After marginalizing over $\Delta\Sigma_0$, the two models give consistent S/N. This is expected as even though the models are somewhat different, both models are effectively marginalizing over the $\Delta\Sigma_0$ as was shown in Eq. (30). For results shown in the paper hereafter we will always marginalize over $\Delta\Sigma_0$ or Σ_0, unless explicitly stated otherwise.

5.1.2 *Impact of r_{cc}*

In Fig. 6 we show the priors used on r_{cc}. Priors labeled as 'small' are computed from the variations in the mean r_{cc} as we vary the satellite fraction in the mock catalogs , while the 'wide' priors are computed by accounting for the noise in r_{cc} (δr_{cc}) as well, i.e., the variations in $r_{cc} \pm \delta r_{cc}$. 'wide' priors are used to test the impact of r_{cc} priors on S_8 and study how parameters change as we loosen the r_{cc} priors. Note that for our fiducial analysis we will use the 'small' priors.

In Fig. 7 we show the impact of various choices of r_{cc} priors on the constraints on S_8. Using the small priors on r_{cc} only makes a small impact on S_8, and both the signal and noise are close to the values obtained by fixing r_{cc} to the correct value for the mock catalogs . Relaxing the r_{cc} priors to 'wide' increases the noise though the best fit values are very similar to the 'small' case. Removing the priors on r_{cc} further, only forcing r_{cc} to be 1 on largest scales, increases the noise further by 20-30% though the best-fitting S_8 values are unchanged (not shown). We also test the results by fixing

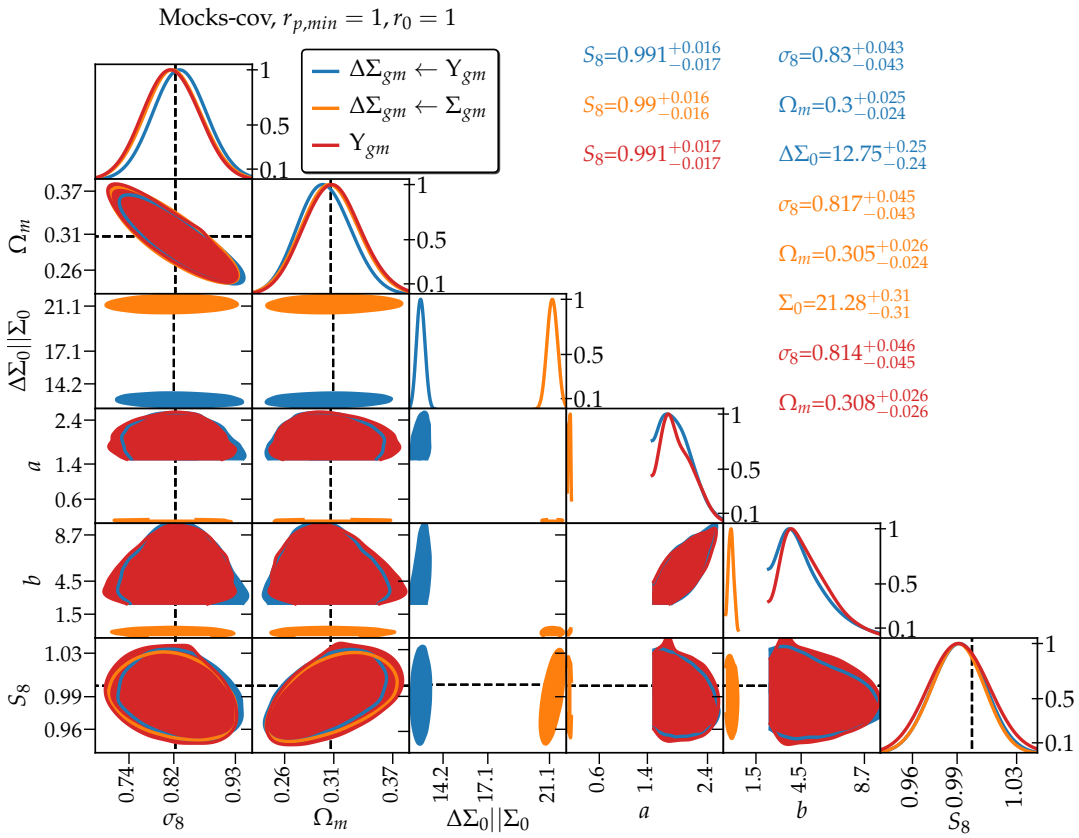

Figure 2. Parameter constraints when fitting the correlation functions from mock galaxy catalogs using different estimators or modeling schemes discussed in section 3, using $r_0 = 1h^{-1}$Mpc. Note that we define $S_8 = \left(\frac{\sigma_8}{0.8228}\right)^{0.8}\left(\frac{\Omega_M}{0.307}\right)^{0.6}$ and its expected value is 1. Blue color represents the modeling of $\Upsilon_{\rm gm}$ as discussed in section 3.1 while red and green show two different methods for modeling $\Delta\Sigma$ by predicting $\Upsilon_{\rm gm}$ or $\Delta\Sigma_{gm}$ as discussed in section 3.2. These results are using with covariance matrix from mock catalogs (no shape noise). We applied flat priors on all parameters, with $\Omega_m \in [0.05, 0.75]$ and $A_s \in [10^{-10}, 10^{-8}]$ (A_s posterior is not shown, instead we show the derived parameter σ_8 based on A_s values in the chain). There were no limits imposed on values of $a, b, \Delta\Sigma_0, \Sigma_0$, but we did impose flat priors on r_{cc} based on the range from mock catalogs which implicitly imposes cuts on a, b, as discussed in section 3. Filled dark contours enclose the 68% region while solid lines enclose the 95% region. Numbers quoted in the figures are the maximum likelihood values while errors bars are from the 16 and 84 percentile. Vertical and horizontal lines mark the fiducial values for different parameters. Note that $\Delta\Sigma_0$ and Σ_0 share the same panel, although they are different parameters that should not be compared numerically. Also, the limits on the panels are determined from the $\pm 3\sigma$ spread (marginal) of the parameter values for all the chains plotted.

r_{cc} to 1 on all scales. This leads to a small bias in the best-fitting values of S_8 though the results are consistent with the fiducial cosmology (with the bias in S_8 being $\sim 0.3\sigma$). This is because $\Delta\Sigma_0$ absorbs most of the effects of the incorrect r_{cc} in this case, and since S_8 is degenerate with $\Delta\Sigma_0$, setting r_{cc} to 1 also increases the noise in S_8 (relative to r_{cc} fixed at correct values).

5.1.3 Effects of theory computation

Troxel et al. (2018) pointed out that for coarse bins the scale at which the theoretical prediction is computed can have an impact on the constraints on cosmological parameters. If these effects become important, then the correct thing to do is to bin the theory predictions using the same weights as data (or use narrower bins). In Appendix D we show that for our results, computing the theoretical prediction at the center of the bin (arithmetic mean) has negligible impact on the cosmological parameters compared to the binned theoretical prediction. Given that we are not sensitive to this choice, for simplicity, all the results shown in the rest of the paper will use the theoretical prediction computed at the central bin value.

5.2 Analysis of real data

In this section we apply our methodology to the galaxy clustering and galaxy-lensing cross correlations presented in Singh et al. (2017a). We use the same pipeline as for the analysis of the mock catalogs, and vary $A_s \in [10^{-10}, 10^{-8}]$, $\Omega \in [0.05, 0.75]$ and r_{cc} with scale-dependent priors derived from the mock catalogs. S_8 is defined as $S_8 = \left(\frac{\sigma_8}{0.8228}\right)^{0.8}\left(\frac{\Omega_M}{0.307}\right)^{0.6}$.

In Fig. 8a we show the cosmological parameter constraints obtained using the BOSS LOWZ sample and galaxy lensing using SDSS data. While the results using different estimators are consistent, there is significant tension with the S_8 from the Planck ΛCDM model due to the data being lower than the predictions from the best-fitting Planck

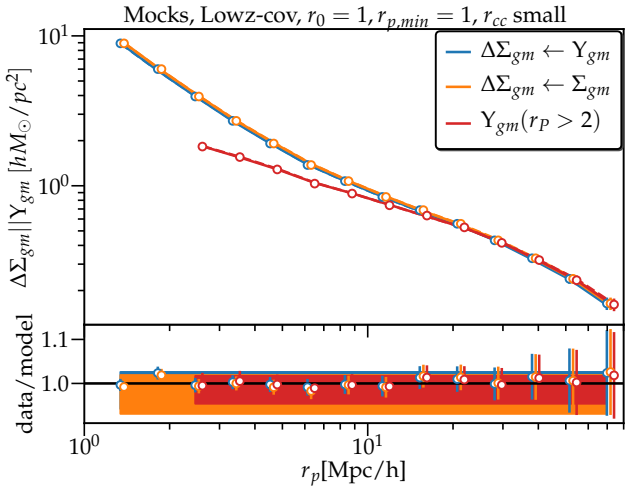

Figure 3. Upper panel: Model fits to the correlation functions from mock galaxy catalogs using best-fitting values (solid lines) from Fig. 2. Open points show the measurements from mock catalogs along with the errors while the solid lines show the best fit model. Dotted lines (not distinguishable form solid lines) are using the maximum likelihood point around the fiducial values of σ_8 and Ω_m (within 0.1% of fiducial values). Note that the errorbars on the points are from the covariance of mock catalogs (no shape noise). Bottom panel: Open points show the ratio of the data points to the model predictions. The filled contours show the ratio of the best fit model to the model from the fiducial (Planck) cosmology, where the contour width indicates the 1σ range on S_8.

Estimator	Model	r_{cc} prior	$S_8 - 1$
Υ_{gm}	Υ_{gm}	small	$-0.01^{+0.016}_{-0.016}$
Υ_{gm}	Υ_{gm}	Fixed	$-0.01^{+0.016}_{-0.015}$
Υ_{gm}	Υ_{gm}	wide	$-0.012^{+0.017}_{-0.015}$
Υ_{gm}	Υ_{gm}	1	$-0.012^{+0.017}_{-0.016}$
$\Delta\Sigma_{gm}$	Υ_{gm}	small	$-0.009^{+0.016}_{-0.017}$
$\Delta\Sigma_{gm}$	Υ_{gm}	1	$-0.008^{+0.016}_{-0.015}$
$\Delta\Sigma_{gm}$	Υ_{gm}	wide	$-0.004^{+0.017}_{-0.017}$
$\Delta\Sigma_{gm}$	Υ_{gm}	fixed	$-0.012^{+0.017}_{-0.016}$
$\Delta\Sigma_{gm}$	Σ_{gm}	small	$-0.01^{+0.016}_{-0.016}$
$\Delta\Sigma_{gm}$	Σ_{gm}	1	$-0.012^{+0.017}_{-0.016}$
$\Delta\Sigma_{gm}$	Σ_{gm}	fixed	$-0.012^{+0.017}_{-0.016}$

Table 2. Table showing the constraints obtained on S_8 in an analysis of the mock catalogs, using different models and r_{cc} prior choices. Constraints using $\Delta\Sigma_{\rm gm}$ are marginalized over $\Delta\Sigma_0$ or Σ_0.

cosmology by $3-4\sigma$. Comparison between the data and the model is shown in Fig. 8b. The best-fitting model agrees well with the data, with no significant deviations; note that the points at large r_p are correlated. The model with the Planck best fitting cosmology, shown by dotted lines, predicts significantly larger $\Delta\Sigma$ and $\Upsilon_{\rm gm}$ relative to the measurements from the data.

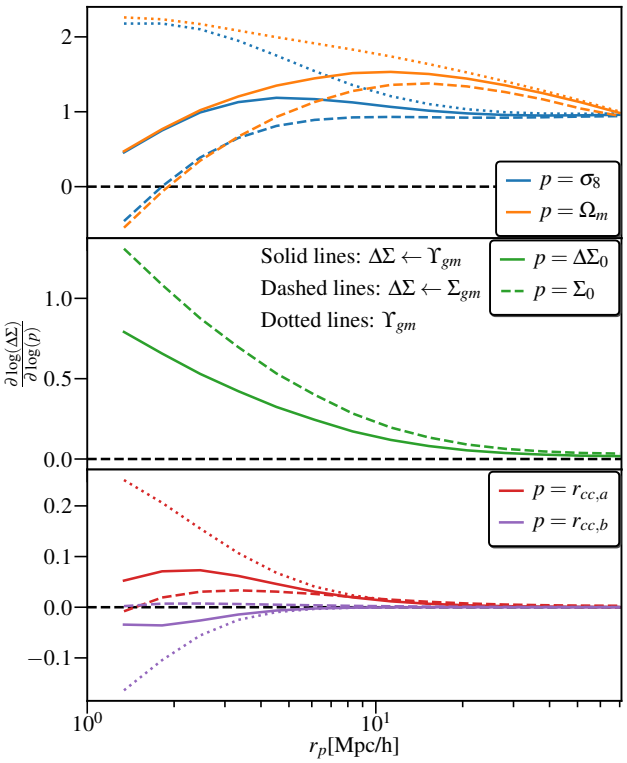

Figure 4. Derivatives of the models with respect to σ_8, Ω_m (upper panel), $\Delta\Sigma_0$ (middle panel) and r_{cc} parameter (lower panel). $\Upsilon_{\rm gm}$is more sensitive to cosmological parameters at smaller scales. However, when including $\Delta\Sigma_0$ into the model, the sensitivity to cosmological parameters decreases at small scales as the impact of $\Delta\Sigma_0$ increases. The scales we use are relatively less sensitive to the r_{cc} parameters.

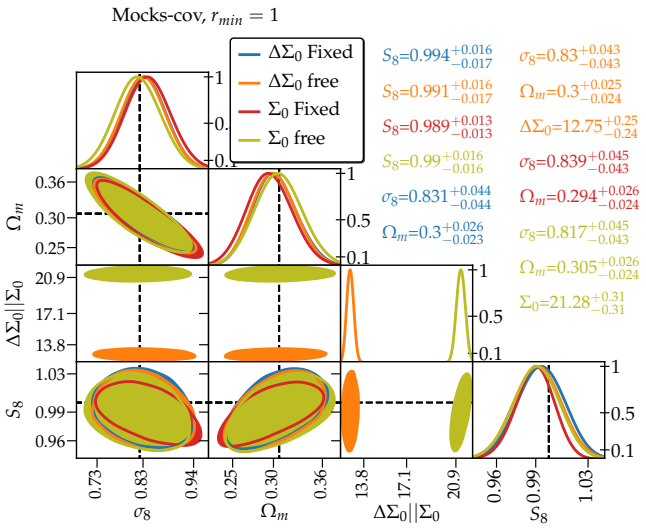

Figure 5. Comparison constraints obtained with fixed $\Delta\Sigma_0/\Sigma_0$ and marginalizing over $\Delta\Sigma_0/\Sigma_0$ for the two models used to fitting $\Delta\Sigma$.

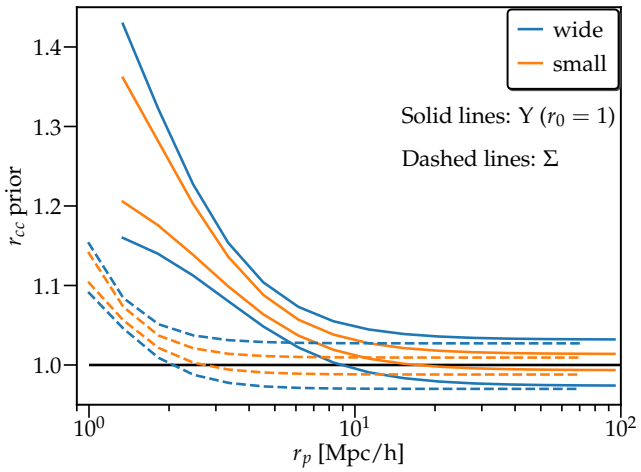

Figure 6. r_{cc} priors obtained from mock galaxy catalogs with different satellite fractions. 'Small' priors are computed using variations in the mean r_{cc} values while the 'wide' priors account for statistical uncertainty also (variations in $r_{cc} \pm \delta r_{cc}$).

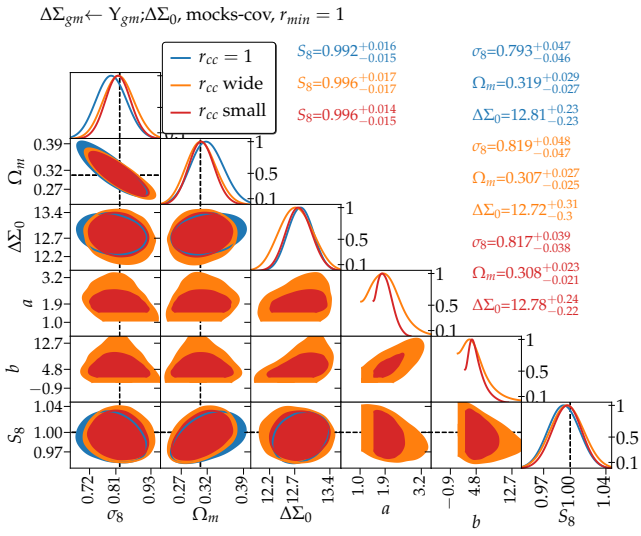

Figure 7. Constraints obtained using different priors on r_{cc}, using covariance from mock galaxy catalogs (no shape noise). All the priors give results consistent with the fiducial cosmology, with $r_{cc} = 1$ having the largest bias $\sim 0.3\sigma$. The constraints using the 'small' priors are tighter compared to those using wide priors by $\sim 20\%$.

The tension observed in Fig. 8a is consistent with the tension observed in the E_G measurements in Singh et al. (2018), though the significance is larger here as the noise in E_G has a significant contribution from the growth rate measurements, which are not included in this work. As was discussed in Singh et al. (2018), there are potential systematic effects in shear calibration and photometric redshifts at the $\sim 6\%$ level, which is comparable to the statistical uncertainties in our results. Even after adding 6% additional systematic uncertainty, we observe $2-3\sigma$ tension with the Planck cosmology. Possible explanations for the residual tension include real tension with Planck due to physics beyond ΛCDM, a statistical fluctuation, or residual non-linear modeling uncertainty (though our analysis of the mock catalogs suggests it is a small effect).

The S/N of the cosmological parameter constraints in our results is lower than that predicted by Wibking et al. (2017), by $\sim 50\%$. This is primarily due to the effects of lower signal relative to the predictions with the Planck cosmology as used by Wibking et al. (2017) (since the covariances are very similar in the two studies) and the Hartlap correction factor when using the jackknife covariance. These effects account for most of the differences $(30-40\%)$ while the remaining differences can arise from the different modeling assumptions as well as the inherent inaccuracies of the Fisher forecasts (they only provide a lower bound on uncertainty in general), making a detailed quantitative comparison difficult.

Fig. 9 shows the results from cross correlations between the BOSS CMASS and LOWZ samples and Planck CMB lensing. For the CMASS sample, we use a larger $r_0 = 4h^{-1}$Mpc, to avoid the scales affected by the Planck beam (see discussion in Singh et al. 2017a). CMB lensing also prefers a low amplitude for S_8, though the noise in these measurements is a factor of 2 larger than in the galaxy lensing and thus are consistent with both the galaxy lensing and the Planck ΛCDM model at the $\sim 1\sigma$ level. In Fig. 9 we also compare our results with the published results using galaxy clustering and galaxy lensing from KiDS (van Uitert et al. 2018) and DES collaborations (DES Collaboration et al. 2017), finding good consistency among all the results (at 95% confidence level).

The choice of scale used in Fig. 8 is fairly aggressive, as we push the analysis into non-linear scales, although the results of the analysis in mock galaxy catalogs is consistent with the expectation. We test the impact of the choice of scale in Fig. 10 by choosing larger r_0 values, as well as restricting the analysis to larger scales for fixed $r_0 = 2h^{-1}$Mpc. While the errors increase with the more conservative choice of r_0 and $r_{p,min}$, the best-fitting values are consistent across the different choices of scales and lower compared with the Planck ΛCDM model. This is consistent with the observation from Fig. 8b, where the data is discrepant with the Planck model at all scales. We choose relatively conservative values of $r_0 = 2h^{-1}$Mpc and $r_{p,min} = 2h^{-1}$Mpc for our fiducial results in the following when comparing with other results in the literature.

For comparison, in Fig. 10 we also plot the S_8 values from recent DES weak lensing results (DES Collaboration et al. 2017) and also from Mandelbaum et al. (2013), who used the same lensing source catalog with a brighter lens sample across the same redshift range. The DES best-fitting cosmological parameter combination, $\sigma_8 \left(\frac{\Omega_M}{0.3}\right)^{0.5} = 0.783^{+0.021}_{-0.025}$, is consistent with our results at the $< 2\sigma$ level (DES $S_8 = 0.925 \pm 0.021$). The results of Mandelbaum et al. (2013), $\sigma_8 \left(\frac{\Omega_M}{0.25}\right)^{0.57} = 0.83 \pm 0.05$ (after rescaling by $1 + m_\gamma \sim 1.04$) are also consistent with our results at $\sim 1\sigma$ level.

In Fig. 11, we show the marginalized constraints on σ_8, Ω_m from Planck 2018 along with some recent large scale structure (LSS) analysis including lensing measurements from this work, DES (DES Collaboration et al. 2017), KiDS (Joudaki et al. 2017) as well as BAO+RSD measurements

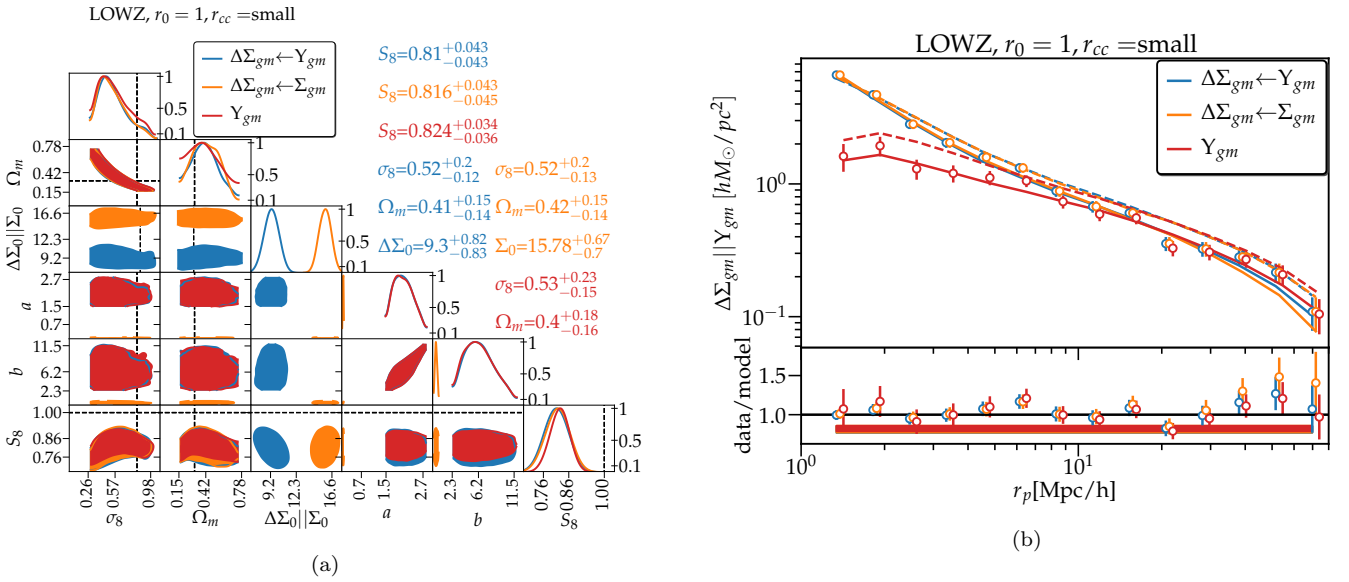

Figure 8. a) Cosmological parameter constraints obtained using LOWZ data with different estimators. We obtain consistent results with different estimators though the results are discrepant with the fiducial cosmology at more than 3σ (stat), though the impact of systematic uncertainties (observational and theoretical) are similar to the statistical errors. Vertical dashed lines show the Planck best-fit values. b) Model fits to the LOWZ data using best-fitting values (solid lines). Dotted lines are using the most likely values of nuisance parameters around the fiducial values of σ_8 and Ω_m. The lower panel show the ratio of data and best-fitting model. The filled contour shows the 1σ range of the best-fitting S_8 relative to the fiducial value of S_8.

from BOSS-DR12 analysis (Alam et al. 2016, chains for RSD+BAO only analysis provided by Shadab Alam). The results obtained by various LSS analysis are consistent with each other though lensing measurements are somewhat discrepant with the marginal constraints obtained from Planck results. Planck results prefer slightly higher S_8 which is driven by the slight preference for larger S_8 in Planck temperature data (see table 2 in Planck Collaboration et al. 2018). In addition to systematic biases, there are physical mechanisms, eg. impact of massive neutrinos, modified gravity or dark energy models beyond Λ which can potentially reduce some of the tension. An analysis of these extensions to the standard ΛCDM model by DES Collaboration et al. (2018) though revealed no significant evidence in favor of these models with the results being limited by the noise in the lensing measurements.

6 CONCLUSIONS

We have presented results using a new method for joint analysis of galaxy clustering and galaxy lensing cross correlations. Since for the current data, galaxy clustering has much better signal to noise compared to the galaxy-lensing cross correlations, we showed that galaxy clustering measurements can be used as part of the model itself, which eliminates the need for complicated galaxy-bias modeling. We still need to model the non-linear cross correlation coefficients, r_{cc}, which we do using a simple parametric model with priors taken from mock catalogs .

We test for the impact of various uncertainties in our theoretical model. In our model, the impact of non-linearities in $\Delta\Sigma$ get absorbed in the nuisance parameter $\Delta\Sigma_0$ and the bias in cosmological parameters (S_8) due to uncertainties in the r_{cc} modeling is around $1-2\%$ depending on the realism of the mock galaxy catalogs. Using the mock galaxy catalogs with a different non-linear physics (higher r_{cc}) compared to the mock catalogs from which the priors on r_{cc} are derived, the bias in S_8 can be $\sim 2\%$. These biases are reduced if we choose a larger r_0, at the cost of losing some small-scale information. We also test the possible impact of baryonic physics on our models using a toy model based on Illustris simulations (Genel et al. 2014; Dai et al. 2018) to modify the small scale galaxy-matter cross correlations. Our results suggest that most of the impact of baryonic physics is absorbed in the nuisance parameters, but the impact on S_8 can still be up to 2%.

We also derived the constraints on cosmological parameters using data from BOSS spectroscopic samples and galaxy lensing maps from SDSS and CMB lensing maps from Planck. In comparison with predictions using the Planck cosmology ($\sigma_8 = 0.8228$, $\Omega_m = 0.307$), we find our measurements to be lower, with the tension on S_8 being of order 20%, $2-4\sigma$ (stat) for the case of galaxy lensing while CMB lensing being lower by 10% ($\sim 1\sigma$). Our results are consistent with recent lensing measurements from the DES and KiDS surveys at the $\sim 2\sigma$ level or better. Leauthaud et al. (2017) also observed the small scale ($r_p < 10h^{-1}$Mpc) galaxy-lensing cross correlations using CFHTLenS and BOSS-CMASS galaxies to be lower than the predictions from the galaxy mock catalogs designed to match the clustering of CMASS galaxies. They performed test for theoretical uncertainties in modeling the measurements, including the effects of baryons, assembly bias as well as extensions to the base ΛCDM model and found that while any single effect cannot explain the size of the discrepancy, these effects when combined together can lead to differences of the order of observed discrepancy. We also estimate systematic uncertainties for our measurements, with

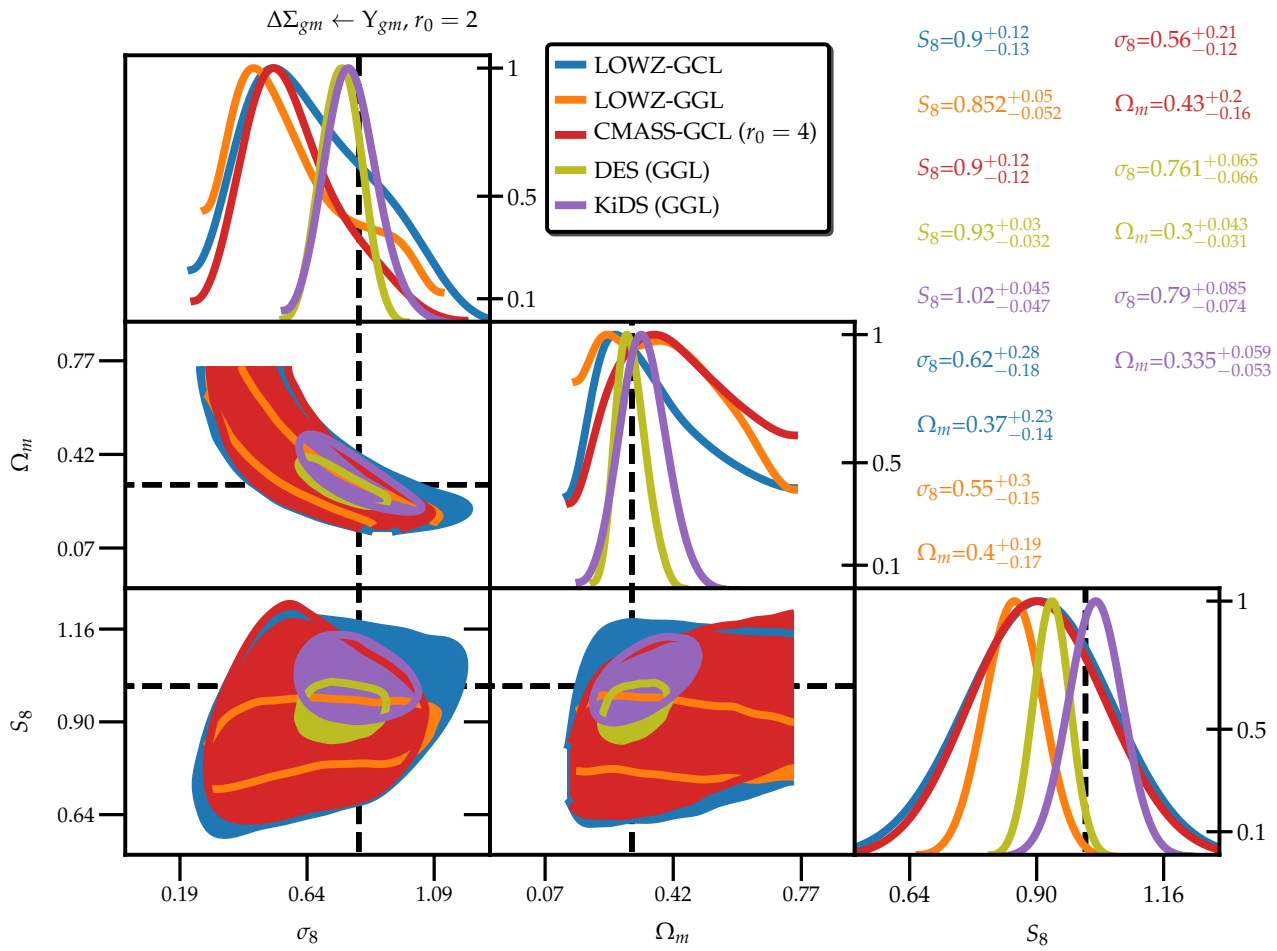

Figure 9. Comparison of constraints obtained using BOSS × CMB lensing (GCL) and galaxy lensing (GGL), along with published galaxy clustering+galaxy-galaxy lensing results from DES Collaboration et al. 2017 and van Uitert et al. 2018 (KiDS×GAMA).

Estimator	Model	r_{cc} prior	S_8	$\chi^2_{\text{best-fit}}$	χ^2_{fid}
Υ_{gm}		small	$0.823^{+0.034}_{-0.035}$	14.79	52.52
Υ_{gm}		1	$0.82^{+0.035}_{-0.037}$	15.08	53.78
Υ_{gm}		wide	$0.824^{+0.035}_{-0.037}$	13.74	52.74
$\Delta\Sigma_{gm}$	Υ_{gm}	small	$0.812^{+0.042}_{-0.044}$	14.57	38.66
$\Delta\Sigma_{gm}$	Υ_{gm}	1	$0.807^{+0.044}_{-0.044}$	15.01	38.98
$\Delta\Sigma_{gm}$	Υ_{gm}	wide	$0.808^{+0.042}_{-0.043}$	13.83	38.71
$\Delta\Sigma_{gm}$ th-cov	Υ_{gm}	small	$0.84^{+0.038}_{-0.04}$	13.0	32.81
$\Delta\Sigma_{gm}$ th-cov	Υ_{gm}	wide	$0.837^{+0.038}_{-0.039}$	12.84	32.13
$\Delta\Sigma_{gm}$	Σ_{gm}	small	$0.816^{+0.043}_{-0.045}$	16.97	35.02

Table 3. Constraints obtained on cosmological parameters ($S_8 = \left(\frac{\sigma_8}{0.8228}\right)^{0.8}\left(\frac{\Omega_M}{0.307}\right)^{0.6}$) using the galaxy-galaxy lensing results (LOWZ×SDSS), with $r_0 = 1h^{-1}$Mpc. 'th-cov' denotes the results obtained using analytical covariance matrix. $\chi^2_{\text{best-fit}}$ shows the minimum χ^2 from the values within the MCMC chains (we use 14 bins in these fits) while χ^2_{fid} show the minimum χ^2 within the chains when $\sigma_8 - \Omega_m$ values are chosen to be within 1% of the Planck values. In case of $\Delta\Sigma$, we do not impose any constraints on $\Delta\Sigma_0$ or Σ_0 when obtaining χ^2_{fid}, which results in better fit on small scales and hence lower χ^2_{fid} (note that small scales also have higher S/N which gives them larger weight in χ^2).

Estimator	Model	r_{cc} prior	S_8	$\chi^2_{\rm best\text{-}fit}$	$\chi^2_{\rm fid}$
Υ_{gm}		small	$0.81^{+0.044}_{-0.046}$	13.73	32.97
Υ_{gm}		1	$0.809^{+0.046}_{-0.046}$	14.06	32.21
Υ_{gm}		wide	$0.799^{+0.052}_{-0.051}$	11.57	32.73
$\boldsymbol{\Delta\Sigma_{gm}}$	Υ_{gm}	small	$0.852^{+0.05}_{-0.052}$	10.99	18.98
$\Delta\Sigma_{gm}$	Υ_{gm}	1	$0.854^{+0.051}_{-0.051}$	10.87	19.06
$\Delta\Sigma_{gm}$	Υ_{gm}	wide	$0.848^{+0.057}_{-0.056}$	11.1	19.55
$\Delta\Sigma_{gm}$ th-cov	Υ_{gm}	small	$0.849^{+0.046}_{-0.047}$	10.92	21.73
$\Delta\Sigma_{gm}$ th-cov	Υ_{gm}	wide	$0.842^{+0.053}_{-0.054}$	10.81	21.58
$\boldsymbol{\Delta\Sigma_{gm}}$- GCL	Υ_{gm}	small	$0.9^{+0.12}_{-0.13}$	3.87	4.84
Υ_{gm}- GCL		small	$0.88^{+0.12}_{-0.12}$	3.62	4.64
$\boldsymbol{\Delta\Sigma_{gm}}$ (CMASS×GCL)	Υ_{gm}	small	$0.93^{+0.15}_{-0.13}$	4.61	5.37
Υ_{gm}	(CMASS×GCL)	small	$0.92^{+0.13}_{-0.11}$	4.14	5.15

Table 4. Same as table 3, now showing fits with $r_0 = 2h^{-1}$Mpc (12 bins). This table presents the fiducial results for our analysis, with the values in bold $\boldsymbol{\Delta\Sigma_{gm}}$ showing the values quoted in abstract (we combined the results for CMB lensing assuming LOWZ and CMASS results are independent). Last four rows show the results with CMB lensing (GCL). $r_0 = 4h^{-1}$Mpc for CMASS×CMB-lensing to avoid the scales below the resolution limit of Planck CMB lensing maps.

up to $\sim 2-3\%$ uncertainty from small scale modeling, $\sim 2\%$ shear calibration uncertainty (multiplicative bias) and $\lesssim 5\%$ due to photo-z calibration uncertainties (Singh et al. 2018). Combined, the systematic error budget on galaxy lensing measurements is $\sim 6\%$, which is comparable to the statistical errors on the measurements. There can also be further systematic contamination in galaxy lensing measurements due to intrinsic alignments, though these have been shown to be consistent with zero at the 5% level (Blazek et al. 2012) for the galaxy lensing sample used in this work.

It is difficult to discern the implications of the tension between our measurements and Planck. It is possible that this is a statistical fluctuation, and it is also possible that the actual amplitude is a bit lower than the central Planck value. Another possibility is that the ΛCDM model is incomplete and extensions including the effects of neutrinos, modified gravity models or extended dark energy models can explain some these tensions. More concerning is the impact of systematic and modeling errors on this method, which remain somewhat difficult to quantify, and which are large comparable to the statistical error. To some extent this is by design: there is a trade-off between the statistical and modeling errors. As we push to smaller scales statistical errors decrease and modeling errors increase, and one chooses the scale where the two are comparable. Still, the optimal choice of this scale remains somewhat model dependent. Even though we have removed all the information from scales below 1-2 Mpc/h and we have quantified the modeling error by comparing to the impact of HOD models on the analysis, it is possible that with a broader HOD parametrization we would need to revisit this. While future measurements with ongoing surveys such as DES, KiDS and upcoming surveys like LSST and Euclid will help in better understanding of systematics, our results highlight the importance of further improving our understanding of theoretical modeling at small scales.

ACKNOWLEDGMENTS

We thank Martin White and Simone Ferraro for useful discussions. We also thank Shadab Alam for providing chains for BOSS DR12 analysis and Chiaki Hikage for providing HSC chains.

This work was supported by NASA grant NNX15AL17G. RM is supported by the Department of Energy Cosmic Frontier program, grant DE-SC0010118.

Funding for SDSS-III has been provided by the Alfred P. Sloan Foundation, the Participating Institutions, the National Science Foundation, and the U.S. Department of Energy Office of Science. The SDSS-III web site is http://www.sdss3.org/.

SDSS-III is managed by the Astrophysical Research Consortium for the Participating Institutions of the SDSS-III Collaboration including the University of Arizona, the Brazilian Participation Group, Brookhaven National Laboratory, Carnegie Mellon University, University of Florida, the French Participation Group, the German Participation Group, Harvard University, the Instituto de Astrofisica de Canarias, the Michigan State/Notre Dame/JINA Participation Group, Johns Hopkins University, Lawrence Berkeley National Laboratory, Max Planck Institute for Astrophysics, Max Planck Institute for Extraterrestrial Physics, New Mexico State University, New York University, Ohio State University, Pennsylvania State University, University of Portsmouth, Princeton University, the Spanish Participation Group, University of Tokyo, University of Utah, Vanderbilt University, University of Virginia, University of Washington, and Yale University.

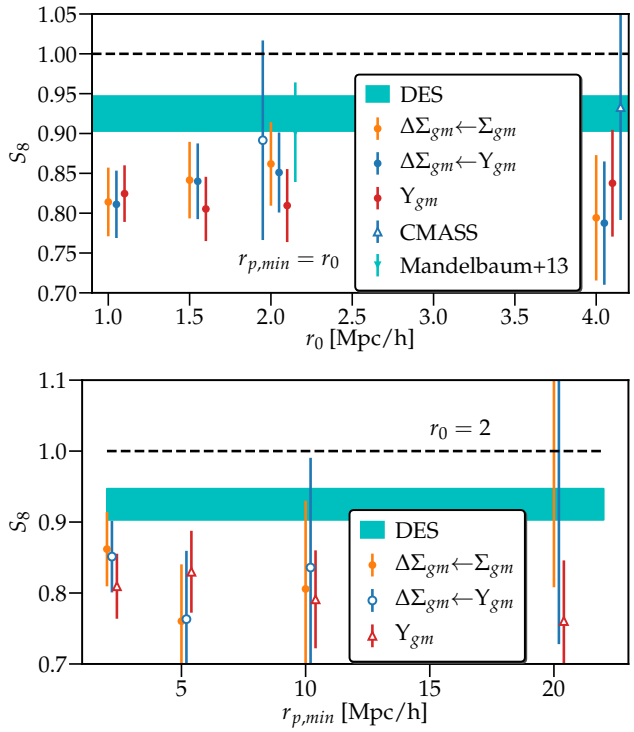

Figure 10. Upper panel: S_8 as function of different r_0. We also show the results from DES (DES Collaboration et al. 2017) and Mandelbaum et al. (2013), where we computed the central value of S_8 using the best-fitting values of Ω_m and σ_8 while the uncertainties shown are computed using relative uncertainties on their values of S_8 (different papers have slightly different definition of S_8.). Lower panel: S_8 as function of different choices of $r_{\rm p,min}$ at fixed $r_0 = 2h^{-1}$Mpc. As the $r_{\rm p,min}$ increases, the constraints on $\Delta\Sigma_0$ weaken, and due to degeneracy between $\Delta\Sigma_0$ and S_8, the constraints on S_8 also weaken. The S_8 value increases at larger $r_{p,min}$ because the $\Delta\Sigma_0$ takes lower values ($\Delta\Sigma_0 \sim -28 \pm 35$ for $r_{p,min} = 20$). In both panels, points with circular markers are using the LOWZ sample, while the point with the triangular marker is using the CMASS sample. Closed markers are using galaxy lensing while open markers are using CMB lensing, and different colors mark the different estimators.

REFERENCES

Abazajian K. N., et al., 2009, ApJS, 182, 543
Ahn C. P., et al., 2012, ApJS, 203, 21
Aihara H., et al., 2011, ApJS, 193, 29
Alam S., et al., 2015, ApJS, 219, 12
Alam S., et al., 2016, preprint, (arXiv:1607.03155)
Alam S., Miyatake H., More S., Ho S., Mandelbaum R., 2017, MNRAS, 465, 4853
Baldauf T., Smith R. E., Seljak U., Mandelbaum R., 2010, Phys.Rev.D, 81, 063531
Bartelmann M., Schneider P., 2001, Phys.Rep., 340, 291
Behroozi P. S., Wechsler R. H., Wu H.-Y., 2013, ApJ, 762, 109
Bernardeau F., Colombi S., Gaztañaga E., Scoccimarro R., 2002, Phys.Rep., 367, 1
Bernstein G. M., Jarvis M., 2002, AJ, 123, 583
Blake C., et al., 2016, MNRAS, 456, 2806
Blanton M. R., Lin H., Lupton R. H., Maley F. M., Young N., Zehavi I., Loveday J., 2003, AJ, 125, 2276
Blazek J., Mandelbaum R., Seljak U., Nakajima R., 2012, J. Cosmology Astropart. Phys., 5, 41
Bolton A. S., et al., 2012, AJ, 144, 144
Buddendiek A., et al., 2016, MNRAS, 456, 3886
Cacciato M., van den Bosch F. C., More S., Li R., Mo H. J., Yang X., 2009, MNRAS, 394, 929
Cacciato M., van den Bosch F. C., More S., Mo H., Yang X., 2013, MNRAS, 430, 767
Conroy C., Wechsler R. H., Kravtsov A. V., 2006, ApJ, 647, 201
Cooray A., Hu W., 2001, ApJ, 554, 56
DES Collaboration et al., 2017, preprint, (arXiv:1708.01530)
DES Collaboration et al., 2018, preprint, (arXiv:1810.02499)
Dai B., Feng Y., Seljak U., 2018, preprint, (arXiv:1804.00671)
Das S., et al., 2011, Physical Review Letters, 107, 021301
Dawson K. S., et al., 2013, AJ, 145, 10
Dvornik A., et al., 2018, MNRAS, 479, 1240
Eisenstein D. J., et al., 2001, AJ, 122, 2267
Fukugita M., Ichikawa T., Gunn J. E., Doi M., Shimasaku K., Schneider D. P., 1996, AJ, 111, 1748
Genel S., et al., 2014, MNRAS, 445, 175
Giannantonio T., et al., 2016, MNRAS, 456, 3213
Gillis B. R., et al., 2013, MNRAS, 431, 1439
Gunn J. E., et al., 1998, AJ, 116, 3040
Gunn J. E., et al., 2006, AJ, 131, 2332
Hand N., et al., 2015, Phys.Rev.D, 91, 062001
Hartlap J., Simon P., Schneider P., 2007, A&A, 464, 399
Heymans C., et al., 2006, MNRAS, 371, L60
Hikage C., et al., 2018, preprint, (arXiv:1809.09148)
Hildebrandt H., et al., 2016, preprint, (arXiv:1606.05338)
Hirata C., Seljak U., 2003, MNRAS, 343, 459
Hoekstra H., Yee H. K. C., Gladders M. D., 2004, ApJ, 606, 67
Hogg D. W., Finkbeiner D. P., Schlegel D. J., Gunn J. E., 2001, AJ, 122, 2129
Hudson M. J., et al., 2015, MNRAS, 447, 298
Ivezić Ž., et al., 2004, Astronomische Nachrichten, 325, 583
Joudaki S., et al., 2017, MNRAS, 465, 2033
Kaiser N., 1987, MNRAS, 227, 1
Kaiser N., Squires G., Broadhurst T., 1995, ApJ, 449, 460
Kilbinger M., 2015, Reports on Progress in Physics, 78, 086901
Kirk D., et al., 2016, MNRAS, 459, 21
Kitching T. D., et al., 2014, MNRAS, 442, 1326
Klypin A., Yepes G., Gottlöber S., Prada F., Heß S., 2016, MNRAS, 457, 4340
Kravtsov A. V., Berlind A. A., Wechsler R. H., Klypin A. A., Gottlöber S., Allgood B., Primack J. R., 2004, ApJ, 609, 35
Kwan J., et al., 2016, preprint, (arXiv:1604.07871)
Landy S. D., Szalay A. S., 1993, ApJ, 412, 64
Leauthaud A., et al., 2012, ApJ, 744, 159
Leauthaud A., et al., 2017, MNRAS, 467, 3024
Lesgourgues J., 2011, preprint, (arXiv:1104.2932)
Lupton R., Gunn J. E., Ivezić Z., Knapp G. R., Kent S., 2001, in Harnden Jr. F. R., Primini F. A., Payne H. E., eds, Astronomical Society of the Pacific Conference Series Vol. 238, Astronomical Data Analysis Software and Systems X. p. 269 (arXiv:astro-ph/0101420)
Mandelbaum R., 2017, preprint, (arXiv:1710.03235)
Mandelbaum R., et al., 2005, MNRAS, 361, 1287
Mandelbaum R., Hirata C. M., Ishak M., Seljak U., Brinkmann J., 2006, MNRAS, 367, 611
Mandelbaum R., et al., 2011, MNRAS, 410, 844
Mandelbaum R., Slosar A., Baldauf T., Seljak U., Hirata C. M., Nakajima R., Reyes R., Smith R. E., 2013, MNRAS, 432, 1544
Massey R., et al., 2007, ApJS, 172, 239
More S., Miyatake H., Mandelbaum R., Takada M., Spergel D. N., Brownstein J. R., Schneider D. P., 2015, ApJ, 806, 2
Nuza S. E., et al., 2013, MNRAS, 432, 743
Omori Y., et al., 2017, ApJ, 849, 124
Padmanabhan N., et al., 2008, ApJ, 674, 1217
Pier J. R., Munn J. A., Hindsley R. B., Hennessy G. S., Kent S. M., Lupton R. H., Ivezić Ž., 2003, AJ, 125, 1559
Planck Collaboration et al., 2014a, A&A, 571, A16

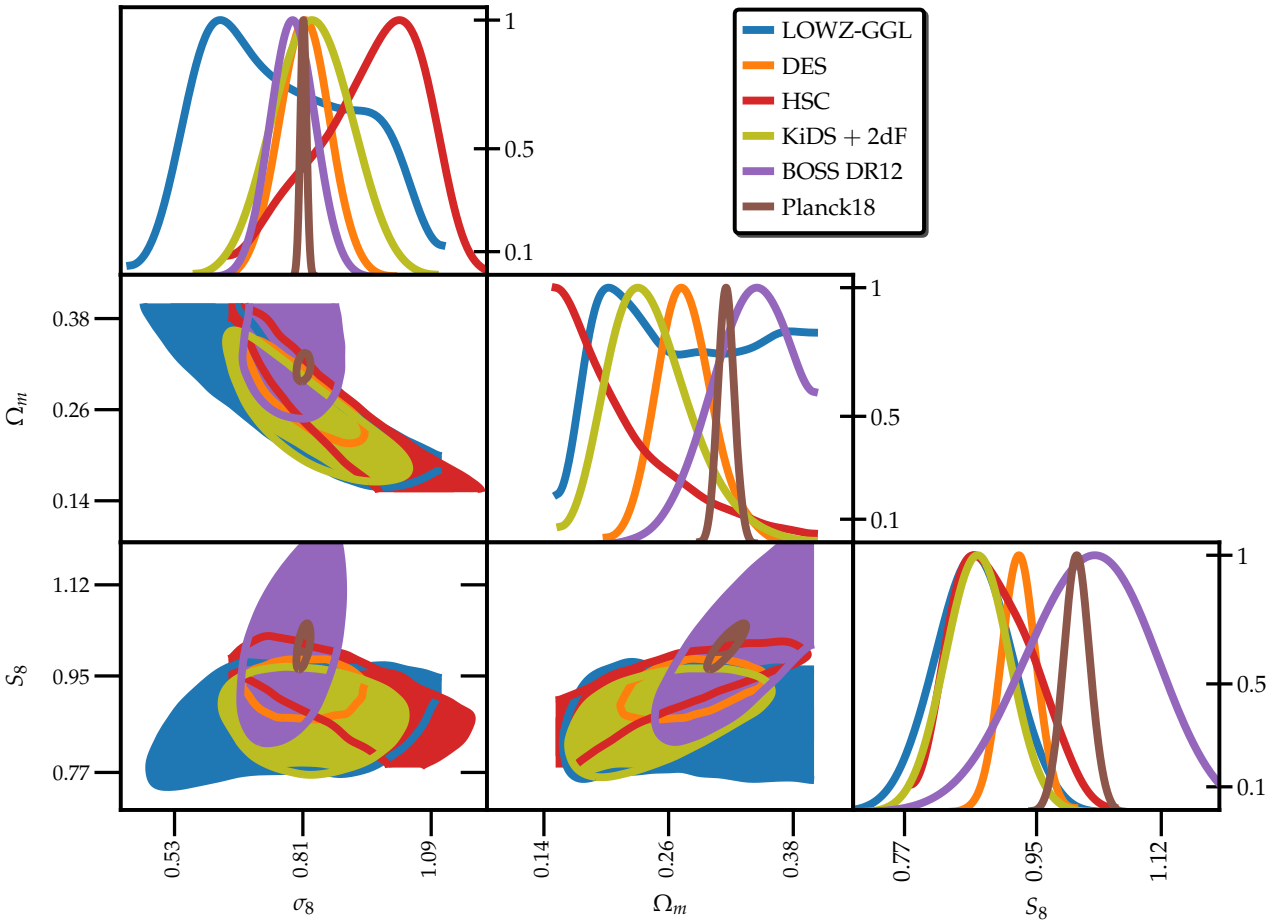

Figure 11. Comparison of Planck 2018 cosmological parameters with results obtained using galaxy-galaxy lensing from SDSS×BOSS (this work, $r_0 = 2h^{-1}$Mpc), KiDS cosmic shear+KiDS×2dFLens+KiDS×BOSS (labeled KiDS+2dF) $S_8 = 0.87 \pm 0.04$ (Joudaki et al. 2017), DES 3X2 analysis, $S_8 = 0.925 \pm 0.021$ (cosmic shear+galaxy-galaxy lensing+galaxy clustering DES Collaboration et al. 2017) and HSC cosmic shear analysis, $S_8 = 0.89 \pm 0.05$ (Hikage et al. 2018). Posteriors from different datasets overlap at 95% level, with slight preference for higher S_8 in Planck posterior being driven by Planck temperature data (see table 2 in Planck Collaboration et al. 2018).

Planck Collaboration et al., 2014b, A&A, 571, A17
Planck Collaboration et al., 2015, preprint, (arXiv:1502.01591)
Planck Collaboration et al., 2018, preprint, (arXiv:1807.06209)
Pullen A. R., Alam S., He S., Ho S., 2016, MNRAS, 460, 4098
Reddick R. M., Wechsler R. H., Tinker J. L., Behroozi P. S., 2013, ApJ, 771, 30
Reid B. A., Seo H.-J., Leauthaud A., Tinker J. L., White M., 2014, MNRAS, 444, 476
Reyes R., Mandelbaum R., Seljak U., Baldauf T., Gunn J. E., Lombriser L., Smith R. E., 2010, Nature, 464, 256
Reyes R., Mandelbaum R., Gunn J. E., Nakajima R., Seljak U., Hirata C. M., 2012, MNRAS, 425, 2610
Richards G. T., et al., 2002, AJ, 123, 2945
Rodríguez-Torres S. A., et al., 2016, MNRAS, 460, 1173
Ross A. J., et al., 2012, MNRAS, 424, 564
Saito S., et al., 2016, MNRAS, 460, 1457
Seljak U., et al., 2005, Phys.Rev.D, 71, 043511
Semboloni E., et al., 2006, A&A, 452, 51
Shan H., et al., 2017, ApJ, 840, 104
Sheldon E. S., et al., 2004, AJ, 127, 2544
Sherwin B. D., et al., 2017, Phys.Rev.D, 95, 123529
Sifón C., et al., 2015, MNRAS, 454, 3938
Singh S., Mandelbaum R., Brownstein J. R., 2017a, MNRAS, 464, 2120
Singh S., Mandelbaum R., Seljak U., Slosar A., Vazquez Gonzalez J., 2017b, MNRAS, 471, 3827
Singh S., Alam S., Mandelbaum R., Seljak U., Rodriguez-Torres S., Ho S., 2018, preprint, (arXiv:1803.08915)
Smee S. A., et al., 2013, AJ, 146, 32
Smith J. A., et al., 2002, AJ, 123, 2121
Springel V., et al., 2018, MNRAS, 475, 676
Strauss M. A., et al., 2002, AJ, 124, 1810
Takahashi R., Sato M., Nishimichi T., Taruya A., Oguri M., 2012, ApJ, 761, 152
Tinker J. L., George M. R., Leauthaud A., Bundy K., Finoguenov A., Massey R., Rhodes J., Wechsler R. H., 2012, ApJ, 755, L5
Tinker J. L., et al., 2017, ApJ, 839, 121
Troxel M. A., et al., 2018, preprint, (arXiv:1804.10663)
Tucker D. L., et al., 2006, Astronomische Nachrichten, 327, 821
Velander M., et al., 2014, MNRAS, 437, 2111
Weinberg D. H., Mortonson M. J., Eisenstein D. J., Hirata C., Riess A. G., Rozo E., 2013, Phys.Rep., 530, 87
Wibking B. D., et al., 2017, preprint, (arXiv:1709.07099)
York D. G., et al., 2000, AJ, 120, 1579
Zhang P., Liguori M., Bean R., Dodelson S., 2007, Physical Review Letters, 99, 141302
van Uitert E., Hoekstra H., Schrabback T., Gilbank D. G., Gladders M. D., Yee H. K. C., 2012, A&A, 545, A71

van Uitert E., et al., 2016, MNRAS, 459, 3251
van Uitert E., et al., 2017, preprint, (arXiv:1706.05004)
van Uitert E., et al., 2018, MNRAS, 476, 4662

APPENDIX A: ANALYSIS WITH DIFFERENT SETS OF MOCK GALAXY CATALOGS

In this appendix we show the result of applying our analysis method to a different set of mock galaxy catalogs that were generated by Reid et al. (2014) (Med-Res mocks) to match the clustering of the BOSS galaxy samples.

In the analysis use the same r_{cc} priors that were derived from the mock galaxy catalogs used in the main part of the paper. The mock catalogs from Reid et al. (2014) have slightly different (higher) non-linear effects compared to the main mock galaxy catalogs, as was shown in Singh et al. (2018). As a result, in Fig. A1 when using a low r_0 value of $1h^{-1}$Mpc, the results are biased by $\sim 2\%$, while the bias is negligible for $r_0 = 2h^{-1}$Mpc. For our main results we will quote the cosmological parameters using both $r_0 = 1h^{-1}$Mpc and $r_0 = 2h^{-1}$Mpc.

In Fig. A2 we show the constraints obtained by varying the satellite fraction using the mock catalogs described in Section 4.2. We obtain consistent values of cosmological parameters (within 1σ) with these mock catalogs, as expected since the primary effect of varying satellite fraction will be to change r_{cc} which for these mock catalogs is accounted for in the width of our priors.

Note choosing higher r_0 decreases the bias on S_8 which is the main parameter constrained using galaxy-lensing cross correlations. Due to different scale dependence of r_{cc}, marginalized constraints on σ_8 and Ω_m can still be somewhat biased as the wrong scale dependence of r_{cc} is compensated by varying Ω_m values. We observe these biases to be present at low levels ($\lesssim 1\sigma$ level on σ_8 and Ω_M), though there could be some contribution from (correlated) noise also in these. These biases are much smaller than the statistical uncertainties in our results using lensing maps and removal of these biases will require more realistic and precise mock galaxy catalogs than have been used in this work.

APPENDIX B: IMPACT OF COVARIANCE

In Fig. B1 we show the comparison of constraints obtained using different covariance matrices. When using the mock catalogs covariance, we get the tightest constraints on the cosmological parameters as the mock catalogs covariance does not include shape noise and it also optimally weighs the data points. Shape noise increases the measurement covariance, especially the diagonal part of the covariance at small scales and hence reduces the information from these scales, increasing the cosmological parameter covariance. We also compare the impact of using data covariance from jackknife and the data covariance from theoretical predictions. Since the jackknife covariance is estimated from 100 regions, we apply the Hartlap correction (Hartlap et al. 2007) to it, which increases the parameter errors by $\sim 10\%$. There is a further difference between the jackknife and theoretical covariance with the diagonal entries of theoretical covariance being lower by $\sim 5\%$. As discussed in Singh et al. (2017b), this is likely due to some contribution from noise in the jackknife covariance and also the fact that in computing the theoretical covariance we do not include the potential contributions from the systematics, which can contribute to the jackknife covariance even if removed from the mean signal. There can also potentially be some impact from non-Gaussian and super-sample covariance terms. Since the mean values of cosmological parameters obtained using different covariances is consistent, our main results using the data will be computed using the jackknife covariance though we will check the results using theoretical covariance as well.

APPENDIX C: IMPACT OF BARYONIC PHYSICS

The effects of baryonic physics tend to modify the matter distribution within and around dark matter halos, modifying the small-scale correlations. To estimate the impact of such changes, we compute the ratio of the projected matter distribution around halos in dark matter-only and Illustris simulations (Genel et al. 2014) using halo profiles provided by Dai et al. (2018), as shown in Fig. C1a. Using this ratio, we then modify the galaxy-matter cross correlations computed from the mock catalogs and then perform the cosmological analysis using the mock catalog covariance. As shown in Fig. C1b, most of the impact of baryons is absorbed in $\Delta\Sigma_0$ and r_{cc}, and the constraints on S_8 change by $\sim 2.5\%$. When using the data covariance, the shape noise downweights the small scales more and the impact of baryonic physics is further reduced in the cosmological parameter. We also note that we are using the Illustris simulation, for which the AGN feedback is likely too strong (Springel et al. 2018), and hence has a significant impact of baryons out to scales larger than seen in other hydrodynamical simulations. We expect the impact of baryonic physics to be smaller than this estimate. Nevertheless, the results in Fig. C1 suggest that future works using better weak lensing measurements may need to model the baryonic physics more carefully in order to achieve unbiased constraints at better than 1% accuracy.

APPENDIX D: EFFECTS OF BINNING

The measured correlation function in bins is an average weighted by the available number of pairs at each scale. The number of pairs scale with the volume in the bin modulated by the effects of the survey window function. The binned projected correlation function is

$$\widehat{\Delta\Sigma}_i = \frac{\int_{r_{p,low}}^{r_{p,high}} \mathrm{d}r'_p r'_p W(r'_p)\Delta\Sigma(r'_p)}{\int_{r_{p,low}}^{r_{p,high}} \mathrm{d}r'_p r'_p W(r'_p)} \tag{D1}$$

where $\Delta\Sigma_i$ refers to the $\Delta\Sigma$ value measured in bin i with $r_{p,high}, r_{p,low}$ marking the limits of the bin. $W(r_p) \in [0,1]$ is the effect of the survey window, with $W(r_p) < 1$ implying that some pairs at r_p are missed relative to the expected scaling due to the effects of the window. We estimate $W(r_p)$ using the pair counts involving random lenses (random-source pairs for galaxy-lensing cross correlations) in the bins as

$$W(r_p) = \frac{\widehat{N}_p}{N_{\rm lens}\overline{n}_{\rm source}\int_{r_{p,low}}^{r_{p,high}} \mathrm{d}r'_p r'_p} \tag{D2}$$

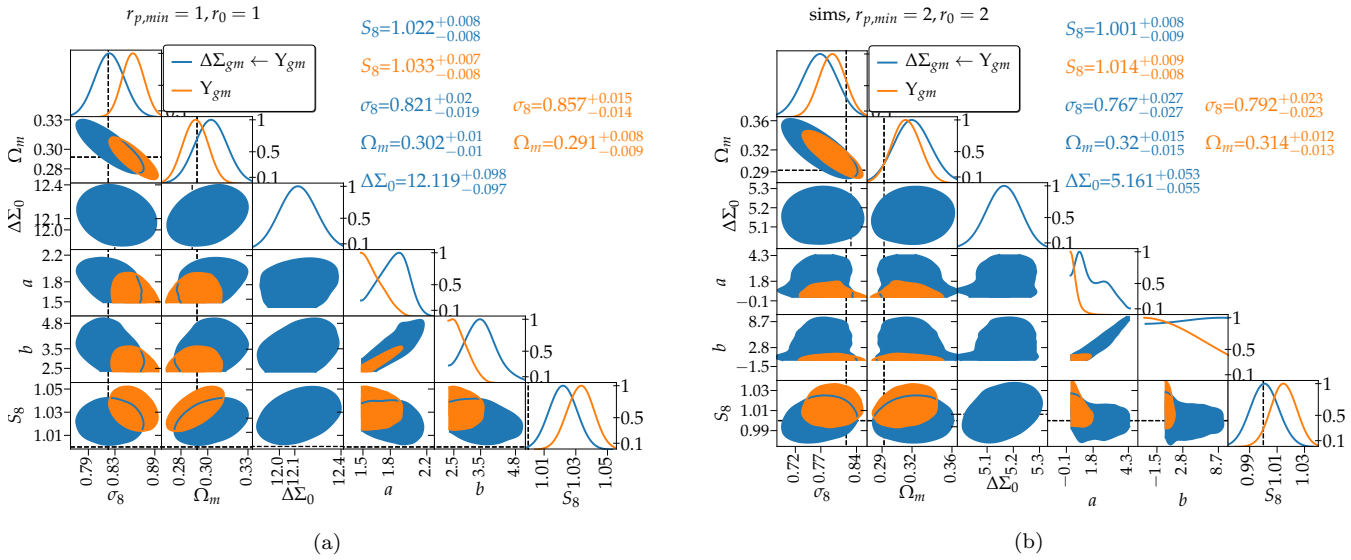

(a) (b)

Figure A1. Parameter constraints for a different set of mock catalogs, Mid-Res in Reid et al. 2014, using the same r_{cc} priors as for the main analysis. For $r_0 = 1h^{-1}$Mpc (left panel), the S_8 constraints are biased by $\sim 2-3\%$ ($\sim 3\sigma$), but for $r_0 = 2h^{-1}$Mpc (right panel) we recover the correct cosmological parameters. Note that for this plot, we defined $S_8 = \left(\frac{\sigma_8}{0.82}\right)^{0.8}\left(\frac{\Omega_m}{0.292}\right)^{0.6}$, where the σ_8 and Ω_m normalization factors correspond to the cosmology of simulations used to generate these mock catalogs.

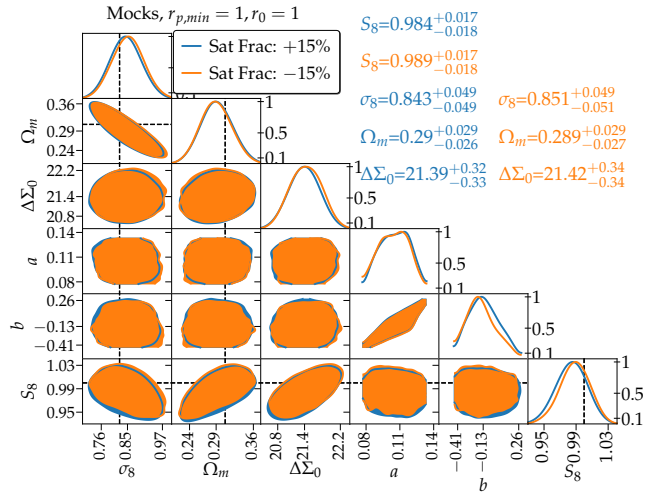

Figure A2. Comparison of constraints obtained using the redshift-dependent mock galaxy catalogs described in Section 4.2 but with different satellite fractions. We obtain consistent results, within 1σ of the fiducial values.

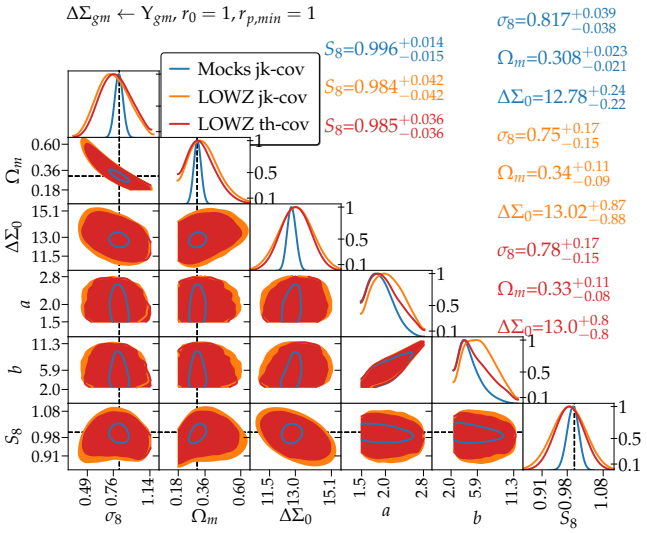

Figure B1. Comparison of constraints obtained using different covariance matrices: the jackknife covariance from mock catalogs (mocks-jk, no shape noise), the jackknife covariance from the data (LOWZ-jk, includes shape noise) and the theoretical prediction for the data covariance (LOWZ-th). The mock catalogs covariance gives the smallest covariance on parameters since it does not include the shape noise. The data covariance including shape noise increases the parameter errors by a factor of ~ 3 as shape noise reduces information especially from small scales.

where $\widehat{N}_p$ is the measured number of pairs and denominator is the expected number of pairs ignoring the window effects. When estimating $W(r_p)$, we divide the number of pairs with the bin volume $\int dr_p r_p$ and then set the $W(r_p)$ at the smallest scale to 1. This does not affect our calculations as the absolute normalization of $W(r_p)$ within the bin cancels out when binning the theory (this is not true for covariance) and the effects we study here are due to the gradient of $W(r_p)$ within the bin. Finally we fit a smooth function to the estimated $W(r_p)$ in the bins to get $W(r_p)$ as function of scale, r_p. $W(r_p)$ for galaxy-galaxy lensing using the LOWZ sample is shown in Fig. D1.

In Figure D2 we show the differences between the binned theoretical predictions and those computed at various effective scales in the bins, including the arithmetic mean ($\overline{r}_p$), the geometric mean ($\overline{r}_{p,\mathrm{geometric}}$),

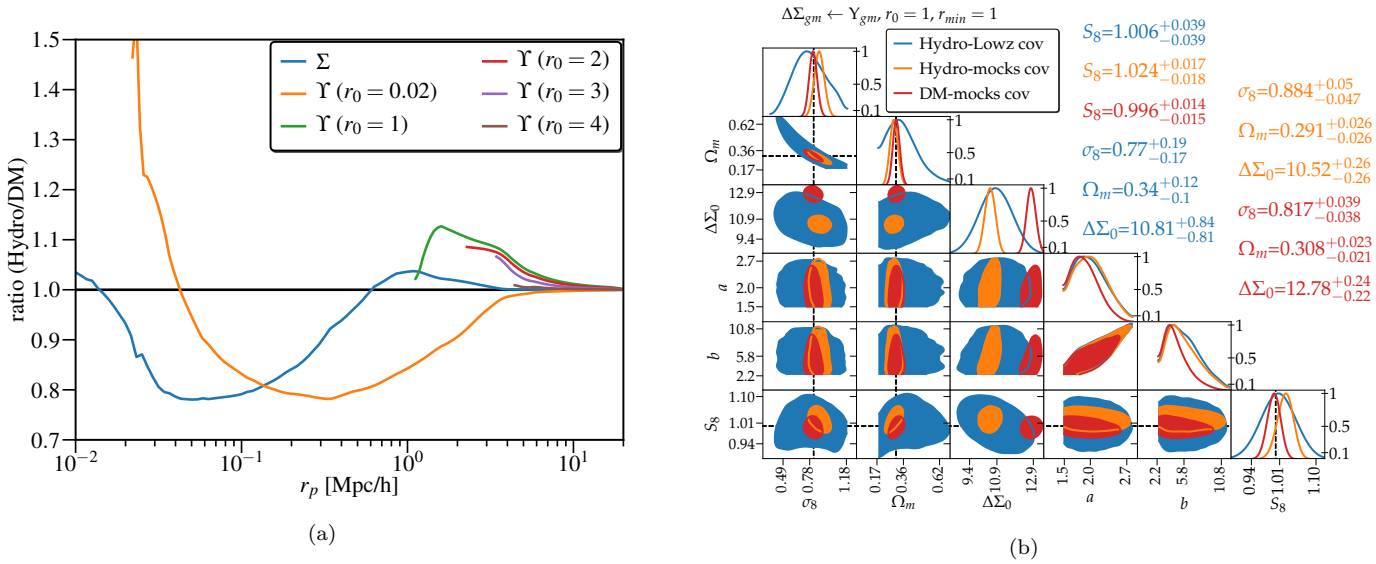

Figure C1. a) The ratio of the projected matter distribution (projected galaxy-matter cross correlation) in and around halos between Illustris hydrodynamical and dark matter only simulations. We use this ratio to modify the galaxy-matter cross correlation signal to study the impact of baryonic physics on cosmological parameter inferences. b) Parameter inferences when using the galaxy-matter cross correlations from mock catalogs (DM) and the modified galaxy-matter cross correlations using the ratio from (a). While the impact of baryonic physics changes the galaxy-matter cross correlations significantly at small scales, most of the effects of these changes are absorbed in $\Delta\Sigma_0$ and r_{cc}. When using the mock catalogs covariances, the S_8 changes by $\sim 2\sigma$ ($\sim 2.5\%$), which suggests that baryonic physics can be important. However, when using the data covariance, which downweights the small scales due to shape noise, these effects are much smaller.

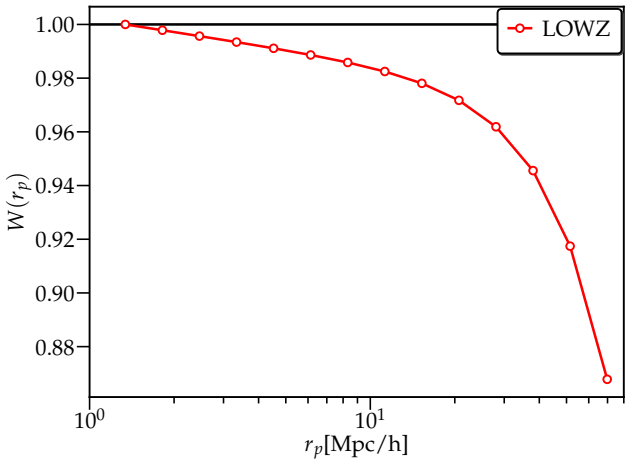

Figure D1. The survey window function $W(r_p)$ for $\Delta\Sigma$ measured using random-source pair counts, with the value at the smallest bin normalized to 1.

and the pair-weighted mean ($\overline{r}_{p,\text{pair-weighted}}$) defined as

$$\overline{r}_p = \frac{r_{p,high} + r_{p,low}}{2} \tag{D3}$$

$$\overline{r}_{p,\text{geometric}} = \sqrt{r_{p,high} \times r_{p,low}} \tag{D4}$$

$$\overline{r}_{p,\text{pair-weighted}} = \frac{\int_{r_{p,low}}^{r_{p,high}} \mathrm{d}r'_p r'^2_p W(r'_p)}{\int_{r_{p,low}}^{r_{p,high}} \mathrm{d}r'_p r'_p W(r'_p)} \tag{D5}$$

The impact of different choices of effective r_p can be understood by the fact that the effective scale of the measurement within the bin depends on the scaling of the pair counts (which also depends on survey window) as well as the scaling of the correlation function. For example, if the function scales as r_p^{-1} and ignoring the effects of the survey window the pair counts scale as r_p, it can be shown that the measurement is effectively made at the arithmetic mean $\overline{r}_p$. The scaling of $\Delta\Sigma$, $\partial \log \Delta\Sigma / \partial \log r_p \sim -1$ (but varies with r_p), explains the result that the theoretical prediction evaluated at the arithmetic mean $\overline{r}_p$ is close to the binned theory, though there are some variations due to the varying slope of $\Delta\Sigma$. The pair-weighted r_p overestimates the effective scale and thus under-predicts the theory while the geometric mean has the opposite effect. Since the survey window tends to down-weight the larger r_p, the effective scale will be smaller than $\overline{r}_p$ for the bins in which the survey window has a large gradient. Thus if we evaluate the model at $\overline{r}_p$, we will be under-predicting the value of the correlation function within the bin. This explains the large discrepancy at larger r_p between the binned models with and without the window effects as well as the model computed at $\overline{r}_p$.

We also note that these effects depend on the size of the bins, with less differences between the choices of effective scale when using smaller bins. While smaller bins may not always be desirable (e.g., covariance estimation is more challenging if there are too many bins), one can always perform the measurement in small bins and then rebin the measurements with the desired weights (which will also require proper treatment in covariance). Also, the choice of effective scale depends on the scaling of the function being measured, and there is no unique choice of effective r_p that works for all functions. The best (and the correct) approach is to bin the theory predictions with proper weights.

Finally, in Figure D3, we show the impact of computing the theoretical prediction at $\overline{r}_p$ compared to the binned theory with mask effects. We find that the final impact on

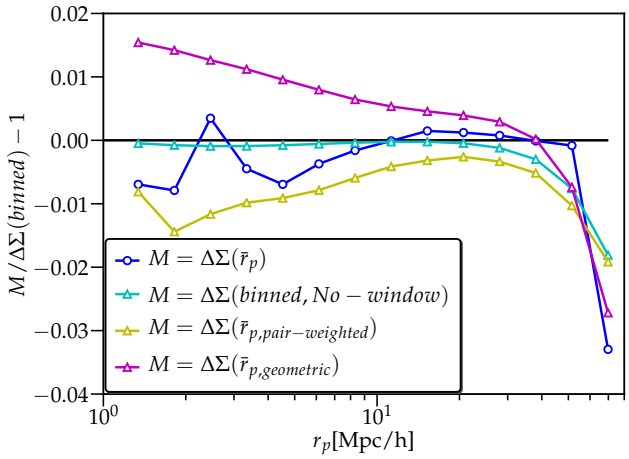

Figure D2. Comparison of the binned theoretical model with the binned model without accounting for effects of window (cyan) and the model computed at different definitions of the central r_p of the bin as described in the Eq. D3-D5.

S_8 is $\sim 0.1\%$ (or $< 0.1\sigma$) on our results with some of the effects on small scales getting absorbed in the r_{cc} and $\Delta\Sigma_0$ parameters.

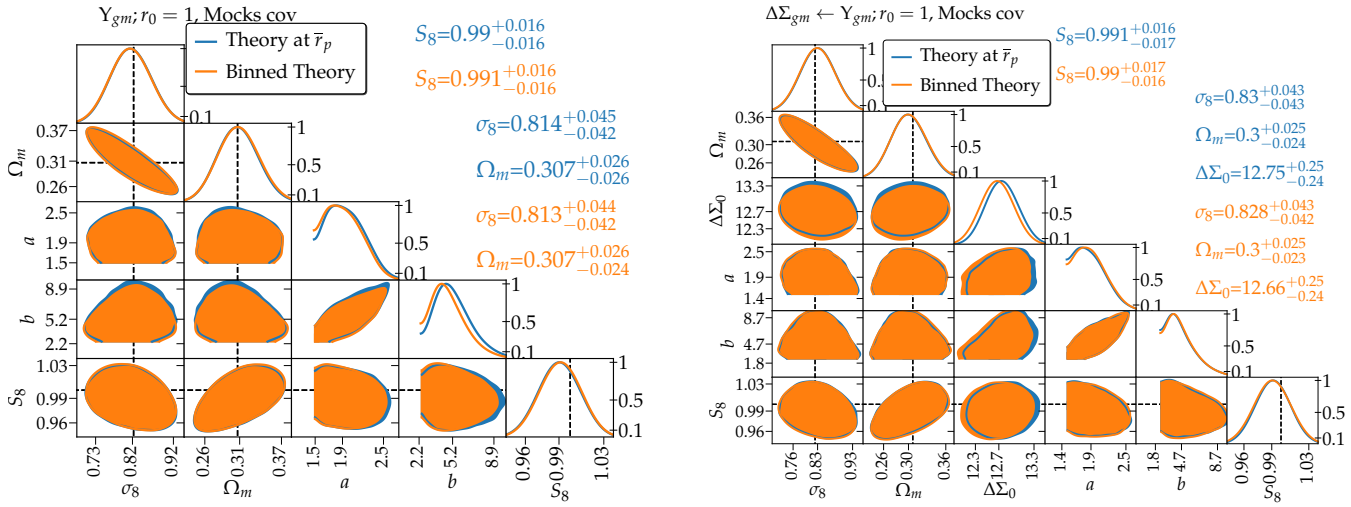

(a) (b)

Figure D3. Comparison of cosmological parameter constraints obtained by binning the theory and computing theory at $\bar{r}_p$. We find negligible difference in the S_8 constraints in the two cases, with some differences getting absorbed in the nuisance parameters.